

The [Y/Mg] chemical clock in the Galactic disk [★]

The influence of metallicity and the Galactic population in the solar neighbourhood

J. Shejeelammal, Jorge Meléndez, Anne Rathsam, and Giulia Martos

Universidade de São Paulo, Instituto de Astronomia, Geofísica e Ciências Atmosféricas, IAG, Departamento de Astronomia, Rua do Matão 1226, Cidade Universitária, 05508-090, SP, Brazil
e-mail: shejeela@usp.br, jorge.melendez@iag.usp.br

Received XXX; accepted YYY

ABSTRACT

Context. Stellar ages are an important parameter in studies of the chemical evolution of the Galaxy. To better estimate these ages, various methods complementary to the conventional isochrone fitting method have been implemented in the past decade. Several recent studies have established the existence of a relationship between chemical clocks and stellar ages. The [Y/Mg] clock is a promising technique, but there are still several open questions, such as its validity for metal-poor stars and differences between the thin and thick disk populations.

Aims. Our aim is to study the relationship between the [Y/Mg] chemical clock and stellar ages for a sample of solar-type disk stars and to provide the empirical dating relation(s) for the stellar age determination from their precise chemical abundances. We also studied the effect of metallicity and populations on this chemical clock.

Methods. We derived precise stellar atmospheric parameters as well as the elemental abundances of Mg and Y through line-by-line differential spectroscopic analysis for a sample of 48 metal-poor solar-type stars based on high-quality, high-resolution ESO/HARPS spectra. From high-precision *Gaia* astrometric data, stellar masses and ages were estimated through isochrone fitting using Yonsei-Yale isochrones. A joint analysis of our sample, together with a sample of 185 solar twins and analogues from our previous works, was performed to calibrate the [Y/Mg] chemical clock in the Galactic disk for $-0.71 \leq [\text{Fe}/\text{H}] < +0.34$. Open clusters and stars with asteroseismic ages were used to validate our relations.

Results. Two different populations are clearly seen in the [Mg/Fe]–[Fe/H] plane: the thick and thin disks. Thick disk stars show an age–metallicity relation, whereas the thin disk shows a flatter age–metallicity distribution. We find a strong, metallicity-dependent anti-correlation between the [Y/Mg] ratio and the stellar ages of our sample. For the first time in the literature, we report similar correlations for thin and thick disk stars.

Conclusions. We find that the [Y/Mg] relation(s) found here for solar-type stars in a wide metallicity range are compatible with those found for solar twins in the literature. Our relation provides high accuracy and precision (0.45 and 0.99 Gyr, respectively) comparable with the best accuracy achieved for solar twins to date.

Key words. stars: abundances – Galaxy: disk – stars: solar-type – solar neighborhood – techniques: spectroscopic

1. Introduction

In addition to precise chemical abundances, the stellar age is an important parameter in studies of Galactic archaeology. Combining accurate age estimates with the existing high-precision abundance data can pave the way to a better understanding of the Galactic chemical evolution (Bland-Hawthorn & Gerhard 2016; Alfredo Collazos 2023). To overcome the problems in the conventional isochrone fitting technique, several complementary methods for precisely determining stellar ages have been investigated in the past decade (e.g. Soderblom 2010; Howes et al. 2019). One such method is the use of chemical clocks – abundance ratios that show a linear relationship with stellar ages (e.g. Nissen 2015; Tucci Maia et al. 2016; Feltzing et al. 2017; Jofré et al. 2020). Also, chemical abundances are being used as part of the training of some machine-learning methods (e.g. Li et al. 2022; Moya et al. 2022; Wang et al. 2024).

da Silva et al. (2012) provided the first evidence of a linear relation between abundance ratios and stellar ages. One of the most studied chemical clocks is the [Y/Mg] ratio, and it has been identified as a potential indicator of age in the case of solar twins (da Silva et al. 2012; Nissen 2015, 2016; Tucci Maia et al. 2016; Spina et al. 2016, 2018). This relation was later found to be valid for solar analogues (Nissen et al. 2017, 2020), solar-metallicity giants (Slumstrup et al. 2017), and red clump stars (Casamiquela et al. 2021) in the solar neighbourhood. Skúladóttir et al. (2019) explored the chemical clock outside the Galaxy and found that [Y/Mg] can be used as a chemical clock in dwarf galaxies.

Feltzing et al. (2017) identified, for the first time, the metallicity dependence of the [Y/Mg] clock and noted that it is valid only for $[\text{Fe}/\text{H}] > -0.5$. The metallicity dependence of the [Y/Mg] chemical clock was later confirmed by Delgado Mena et al. (2018, 2019) and Casali et al. (2020). Casali et al. (2020) first determined that the [Y/Mg]–age relation is not universal and depends on the Galactocentric distance (R_{GC}), which was further investigated by Viscasillas Vázquez et al. (2022). This relation

[★] Based on data obtained from the ESO Science Archive Facility with DOI <https://doi.org/10.18727/archive/33>

has a large dispersion outside the solar neighbourhood (Casali et al. 2020; Casamiquela et al. 2021).

The dependence of the chemical clocks on other parameters, such as stellar mass and temperature, was explored by Delgado Mena et al. (2019). The applicability of the [Y/Mg] clock method to thin and thick disk populations of the Galaxy has also been investigated, and different correlations for these two components have been identified (Delgado Mena et al. 2018; Titarenko et al. 2019; Tautvaišienė et al. 2021). These studies have shown that the chemical clock is applicable only to thin disk stars.

Chemical dating can be closely related to the chemical evolution of the Galaxy and its different components (e.g. Haywood et al. 2013, 2016). The aim of this paper is to study the [Y/Mg]–age relation in the solar neighbourhood of the Galactic disk over a wide metallicity range. Our analysis is based on a combined sample of 233 solar-type stars with metallicities in the range $-0.7 \leq [\text{Fe}/\text{H}] < +0.34$. We examined the metallicity dependence of the [Y/Mg] chemical clock using this sample. Few studies in the literature have explored the relation between [Y/Mg] and stellar ages for thick disks, and the findings are not always consistent; we investigated this as well. This paper is structured as follows: Sect. 2 discusses the stellar sample and the source of high-resolution spectroscopic data. In Sect. 3 we present the spectroscopic analysis. Results are discussed in Sect. 4. Finally, concluding remarks are presented in Sect. 5.

2. Stellar sample and spectroscopic data

Our analysis is based on a sample that contains three classes of stars of different similarity to the Sun: solar twins, solar analogues, and solar-type (solar-like) stars. Solar twins are the stars with parameters $\Delta T_{\text{eff}} = 100$ K, $\Delta \log g = 0.1$ dex, and $\Delta[\text{Fe}/\text{H}] = 0.1$ dex of the solar values (Meléndez et al. 2006; Ramírez et al. 2009). Solar-analogues are the dwarf stars with parameters $\Delta T_{\text{eff}} = 500$ K and $\Delta[\text{Fe}/\text{H}] = 0.3$ dex of the solar values (Soderblom & King 1998; Yana Galarza et al. 2016). Solar-type stars are those similar to the Sun in mass and evolutionary stage, belonging to the F8V to K2V spectral types with a B–V colour in the range 0.5 to 1.0 (Cayrel de Strobel 1996; Soderblom & King 1998).

The stellar sample consists of 48 solar-type Galactic disk stars selected from an updated catalogue of stellar parameters from Ramírez & Meléndez (2005), with parameters $5600 \text{ K} \leq T_{\text{eff}} \leq 6400 \text{ K}$, $4.1 \leq \log g \leq 4.6$, $-0.71 \leq [\text{Fe}/\text{H}] \leq -0.3$, and $0.85 \leq M \leq 1.05 M_{\odot}$. To have a wider metallicity range in the sample, in addition to these 48 metal-poor objects, we included 185 solar twins and analogues ($-0.3 \leq [\text{Fe}/\text{H}] < +0.34$) from our previous studies (Spina et al. 2018; Martos et al. 2023; Rathsam et al. 2023). Thus, our final sample consists of 233 solar-type¹ stars spanning the metallicity range $-0.71 \leq [\text{Fe}/\text{H}] < +0.34$.

For all the stars, the high-resolution spectra at $R \sim 115,000$ acquired using the HARPS (High Accuracy Radial velocity Planet Searcher) spectrograph were taken from the European Southern Observatory (ESO) archive². These spectra cover the wavelength range 3780–6910 Å. Since we need high-quality spectra for a high-precision analysis, we selected multiple spectra of the same objects with individual S/N in the range 30–370. To minimise the effect of telluric contamination on the spectral lines, we used at least five spectra taken on different nights. Then the

spectra were radial velocity corrected using IRAF³, and then combined to get the final spectra. The final S/N of the combined spectra ranges from 360 to ~ 1000 . The combined spectra were normalised by splitting them into seven segments, using IRAF. The continuum normalisation of each individual segment was done iteratively using cubic spline polynomial of similar orders for the same segments, by evaluating the residuals as well as the visual fit to the continuum. Finally, the normalised segments are combined using IRAF. The spectra taken before and after the HARPS upgrade (June 2015) were treated separately due to the difference in the shape of the continuum, and combined afterwards. In addition to the spectra of the stellar sample, we also acquired HARPS solar spectra at the same resolution obtained from the asteroid Vesta.

3. Spectroscopic analysis

The stellar atmospheric parameters as well as the elemental abundances were determined through a line-by-line differential analysis (Meléndez et al. 2012, 2014; Bedell et al. 2014) with respect to the Sun using the Python code q^2 ⁴ (Ramírez et al. 2014), adopting the line list from Meléndez et al. (2014). The equivalent width (EW) of each spectral line is measured on a star-by-star basis, including those in the Sun, performing deblending whenever necessary. For these calculations, q^2 uses the ATLAS9 Kurucz grid of model atmospheres (Castelli & Kurucz 2003) and the *ABFIND* driver of the code MOOG (version 2019; Sneden 1973; Sneden et al. 2012) that employs local thermodynamic equilibrium (LTE).

3.1. Stellar atmospheric parameters

We used the EW measurements of 91 Fe I and 18 Fe II lines to determine the atmospheric parameters. The final atmospheric parameters were determined in an iterative process from the initial guess of parameters using the differential excitation, ionisation, and reduced EW (= EW/ λ) balances. The adopted solar atmospheric parameters are $T_{\text{eff}} = 5777$ K, $\log g = 4.44$ dex, $\zeta = 1$ km s⁻¹, and $[\text{Fe}/\text{H}] = 0$ dex (Cox 2000). The code also evaluates the uncertainty on each atmospheric parameter following the procedures in Epstein et al. (2010) and Bensby et al. (2014), which is the cumulative uncertainty that includes the uncertainty on the measurements as well as the uncertainty that arises due to the mutual dependence of the atmospheric parameters. The typical precisions on the estimated atmospheric parameters of our sample are $\sigma(T_{\text{eff}}) = 10$ K, $\sigma(\log g) = 0.03$ dex, $\sigma(\zeta) = 0.02$ km s⁻¹, and $\sigma([\text{Fe}/\text{H}]) = 0.007$ dex.

Following the determination of the stellar atmospheric parameters and their uncertainties, q^2 automatically uses the appropriate model atmospheres to calculate the chemical abundances using the MOOG code under LTE.

3.2. Chemical abundances: Mg and Y

The abundances of the elements Mg and Y are measured for each star using the same differential EW method as above. All the elemental abundances are scaled relative to those obtained for the Sun on a line-by-line basis. We note that, in all the metal-poor stars, the differential abundance derived from the Mg I 4730.040 Å line is lower by around ~ 0.05 dex compared to other Mg I

¹ Hereafter, we refer to the whole sample as solar-type stars because it contains all the three type stars

² https://archive.eso.org/wdb/wdb/adp/phase3_spectral/form

³ Image Reduction and Analysis Facility; <https://iraf-community.github.io/>

⁴ [qoyllur-quipu; https://github.com/astroChasqui/q2](https://github.com/astroChasqui/q2)

lines. So, to get the consistent abundance values from all the Mg lines, we applied an offset of -4 mÅ to the measured EW of this line in the Sun. The Mg I lines at 6318.717 and 6319.236 Å are contaminated by nearby telluric absorption features in a few stars, and in those cases these lines were not considered in their abundance determination.

Yttrium shows hyperfine splitting, and we took this into consideration when calculating its abundances. It is implemented by q^2 through the *blends* driver in the M00G code and the adopted Y hyperfine lines from the Kurucz database. The mean errors on the estimated abundances of Mg and Y are $\langle\sigma[\text{Mg}/\text{Fe}]\rangle = 0.01$ dex and $\langle\sigma[\text{Y}/\text{Fe}]\rangle = 0.02$ dex, respectively.

3.3. Stellar masses and ages

The masses and ages of the stellar sample were determined using the code q^2 , employing the spectroscopically determined atmospheric parameters and the Yonsei-Yale isochrones (Yi et al. 2001; Kim et al. 2002). Since our stars show non-solar abundances ($[\alpha/\text{Fe}] \neq 0$), the [Fe/H] values do not represent their actual metallicity. Hence, to account for the effect of α -enhancement on the global metallicity of the stars, we applied a correction factor, $+\log_{10}(0.64 \times 10^{[\alpha/\text{Fe}]} + 0.36)$ (Salaris et al. 1993), together with an offset of -0.04 to recover the age and mass of a star with solar parameters, to the [Fe/H], as described in Spina et al. (2018). However, for the stars with [Fe/H] < 0 , the effect of α -enhancement is already incorporated in the Yonsei-Yale isochrones to follow the Galactic trend, using the $[\alpha/\text{Fe}]$ values given in Meléndez et al. (2010). We had to subtract this factor to avoid double α -enhancement. For the stars in the metallicity range $-1 \leq [\text{Fe}/\text{H}] \leq 0$, the value is given by $[\alpha/\text{Fe}] = -0.3 \times [\text{Fe}/\text{H}]$. So, the final global metallicity ([M/H]) of the stars in our sample is given by Eq. 1, where we have used our estimates of [Mg/Fe] as a proxy for $[\alpha/\text{Fe}]$:

$$[\text{M}/\text{H}] = [\text{Fe}/\text{H}] - 0.04 + \log_{10}(0.64 \times 10^{[\text{Mg}/\text{Fe}]} + 0.36) - \log_{10}(0.64 \times 10^{-0.3 \times [\text{Fe}/\text{H}]} + 0.36). \quad (1)$$

The q^2 code produces a probability distribution for stellar masses and ages through an isochrone fitting, where the spectroscopic stellar parameters are compared with those obtained from the grid of isochrones (Ramírez et al. 2014). The most probable values of these probability distributions are adopted as stellar masses and ages, and the $1-\sigma$ range around the most probable values are taken as their respective uncertainties.

For this calculation, we used the parallax values adopted from the *Gaia* DR3⁵ (Gaia Collaboration et al. 2016, 2022; Babusiaux et al. 2022), and the V magnitudes from SIMBAD. If the V magnitudes were not available, then we estimated it using the *Gaia* G magnitudes and (BP - RP) colour indices through the calibration equation given by Rathsam et al. (2023).

The ages and masses of the solar twins from Spina et al. (2018) were recalculated using the same procedure as our sample, for consistency in the analysis, and are listed in Martos et al. (2023). The typical uncertainties in the isochrone ages and masses of the stellar sample are ~ 0.4 Gyr and $0.01 M_{\odot}$, respectively.

4. Results and discussion

Here, we discuss the results of our analysis of the combined sample of 233 disk stars (48 solar-type stars from this study and 185 solar twins and analogues from our previous studies). The estimated stellar atmospheric parameters, masses, ages, and the abundance ratios of our sample are given in Table A.1, and those of solar twins and analogues are given in Table A.2. The parameters of the combined sample are $5149 \text{ K} \leq T_{\text{eff}} \leq 6210 \text{ K}$, $4.04 \leq \log g \leq 4.57$, $-0.71 \leq [\text{Fe}/\text{H}] < 0.34$, and $0.82 \leq M \leq 1.1 M_{\odot}$, and all the stars lie in the solar neighbourhood ($R_{GC} \sim 8$ kpc).

4.1. Bi-modality of the Galactic disk and age–metallicity relation

Figure 1 shows the [Mg/Fe] ratio with respect to the [Fe/H] of the combined sample. From this figure, we can clearly see two populations of [Mg/Fe] at low-metallicity, the high- α or thick disk and the low- α or thin disk. At higher metallicities ($[\text{Fe}/\text{H}] \geq 0$), both populations are indistinguishable. This bimodality of the Galactic disk in the $[\alpha/\text{Fe}]$ - [Fe/H] plane has already been identified in several previous studies (e.g. Reddy et al. 2006; Adibekyan et al. 2011, 2012; Haywood et al. 2013; Nidever et al. 2014; Bensby et al. 2014; Ness et al. 2019; Weinberg et al. 2019; Xiang & Rix 2022; Leung et al. 2023; Imig et al. 2023; Patil et al. 2023). It is the consequence of different chemo-dynamical evolution and star formation history of the Milky Way disk (e.g. Haywood et al. 2013; Bergemann et al. 2014; Casagrande et al. 2011). Generally, thick disk is composed of old, metal-poor, α -enhanced stars, whereas thin disk is composed of younger, α -poor stars (Fuhrmann 1998; Bensby et al. 2005; Lee et al. 2011). However, there is no obvious method for completely disentangling these two components of the Galactic disk and to identify purely thin or thick disk stars in the solar neighbourhood (Bensby et al. 2003; Adibekyan et al. 2012; Haywood et al. 2013). Furthermore, the separation between the α -sequences and even the existence of boundary between these two populations (Bovy et al. 2012a) are still topics of debate. A detailed review on Galactic disk can be found in Rix & Bovy (2013).

Previously, the thin and thick disk stars were distinguished either from a pure kinematical approach (e.g. Bensby et al. 2003; Reddy et al. 2006) or from an approach that combines kinematics, metallicity, and age (e.g. Haywood 2008). However, both these methods are found to be prone to ‘contamination’ or overlap between the two components (Bensby et al. 2003; Adibekyan et al. 2012; Bovy et al. 2012b). In addition to this, the radial migration is proposed to have redistributed the stars in the solar neighbourhood (e.g. Liu & van de Ven 2012; Haywood et al. 2013). This radial migration and the higher eccentric orbits lead to the contamination of the kinematically selected thin and thick disk stars in the solar vicinity (e.g. Schönrich & Binney 2009).

The advent of several large sky multi-object spectroscopic surveys in the last decade allowed the chemo-kinematic analysis of much larger samples of stars. As a consequence, a purely chemical approach to dissecting the Galactic disk began to gain significance. Several studies have shown that chemical dissection of the Galactic disk is more reliable because the chemical composition of a star is a more stable property that is closely related to the time and place of birth, whereas the kinematics and spatial positions change all the time (Navarro et al. 2011; Adibekyan et al. 2011; Liu & van de Ven 2012; Bovy et al. 2012b; Adibekyan et al. 2012, 2013). It has also been proposed that various properties (scale height, kinematics, etc) of differ-

⁵ <https://gea.esac.esa.int/archive/>

ent Galactic stellar populations can be parametrised using their chemical composition (Bovy et al. 2012b).

For a given age, the solar vicinity exhibits a broader metallicity distribution since stars of different birth radii (and hence different metallicities) contribute to the local neighbourhood (Liu & van de Ven 2012). As a result, despite the fact that the thick disk is comparatively older, stars with a range of ages and metallicities can contribute to both thin and thick disks, giving rise to a large overlap in metallicity. Hence, even though the chemical composition is the more reliable approach, the metallicity ($[\text{Fe}/\text{H}]$) alone is not an ideal choice. From the chemo-orbital analysis of a sample of SDSS/SEGUE data (Sloan Extension for Galactic Understanding and Exploration; Yanny et al. 2009), Liu & van de Ven (2012) showed that the α -abundance is preferred because it is relatively independent of birth radii and is a more appropriate proxy for age. The distribution of the $[\alpha/\text{Fe}]$ ratio with respect to $[\text{Fe}/\text{H}]$ has been used in several studies to distinguish between the two disk populations (e.g. Adibekyan et al. 2011; Haywood et al. 2013). The limit characterising the thin and thick disk populations is defined empirically, by examining the chemical separation in $[\alpha/\text{Fe}]$ between the high- α (thick disk) and low- α (thin disk) sequences. Recent studies based on the chemo-kinematical and statistical methods using large samples from high-resolution spectroscopic surveys, such as Apache Point Observatory Galactic Evolution Experiment (APOGEE; e.g. Anders et al. 2014; Patil et al. 2023), the *Gaia*-ESO Survey (GES; e.g. Gent et al. 2024), and GALactic Archaeology with HERMES (GALAH; e.g. Cantelli & Teixeira 2024), have shown that the decomposition of the Galactic disk is better understood in terms of the chemical enrichment (α abundance).

On the grounds of the above discussion, we adopted the chemical separation given in Adibekyan et al. (2011) to separate the thin and thick disk sequences. This is shown as a solid red line in the $[\text{Mg}/\text{Fe}]$ - $[\text{Fe}/\text{H}]$ plane in Fig. 1. We identified the stars above this line as thick disk stars and those below as thin disk stars⁶. The behaviour of $[\text{Mg}/\text{Fe}]$ ratio with respect to various orbital properties and the Toomre diagram of our sample are shown in Figs. B.1 and B.2. As seen in the several previously mentioned works, our chemically defined thick and thin disk stars are mixed in the kinematic plane. The thick disk contains the older stars (age > 8 Gyr; two stars have ages of 6.7 and 7.5 Gyr) of the sample, whereas the thin disk shows an age spread. All the youngest stars of the sample belong to the thin disk.

We note that a younger star with an age of 4.6 Gyr is a member of the thick disk (cyan circle; Fig. 1 lower panel). This object, HD 65907, shows anomalous behaviour compared to other stars of the sample. As seen in the figures, it lies well off the other objects of its kind. Fuhrmann et al. (2012) analysed this anomalous object, and from its chemical abundance they identified it as an old, population II, thick disk star with an age of 12 or 13 Gyr. However, the age inferred from the evolutionary tracks is $5.6^{+2.2}_{-1.8}$ Gyr, which contradicts its chemical properties. According to Fuhrmann et al. (2012), this discrepancy can only be resolved with a mass accretion scenario on HD 65907. So, this object is probably a product of a former mass-transfer event, like the solar analogue HIP 10725 (Schirbel et al. 2015).

The age–metallicity distribution (AMD) of the whole sample is shown in Fig. 2. Earlier studies found that the age and metallicity are not strongly correlated in the solar neighbourhood, and that the metallicity shows a significant scatter for the same age (e.g. Edvardsson et al. 1993; Feltzing et al. 2001; Hay-

wood 2006; Casagrande et al. 2011; Bensby et al. 2014; Lin et al. 2020; Sahlholdt et al. 2022; Patil et al. 2023). From Fig. 2, it is clear that stars of similar age show a large range of metallicities. The thick disk stars in the sample show an age–metallicity relation (AMR; Fig. 2, upper panel), as previously noted by Schuster et al. (2006), Bensby et al. (2014), Patil et al. (2023), and others. Meanwhile, the age and metallicity are uncorrelated for the thin disk stars, and show an almost flat distribution. However, both the populations are indistinguishable from each other in the age– $[\text{Fe}/\text{H}]$ space.

From the contour plot for the AMD of the stellar sample (bottom panel, Fig. 2), we note the following: (i) up to the age of ~ 12 Gyr and for $[\text{Fe}/\text{H}] > -0.2$, we see a flat AMR with a scatter in the metallicity; (ii) for the older (age > 7 Gyr), metal-poorer stars in the sample ($[\text{Fe}/\text{H}] < -0.2$), we see a downward trend in the AMD; and (iii) the majority of the distribution is centred at $[\text{Fe}/\text{H}] \sim 0$ with a peak around ages between 4 - 9 Gyr. This is in par with the findings in the previous studies of the Galactic disk (e.g. Edvardsson et al. 1993; Feltzing et al. 2001; Bergemann et al. 2014). The AMR and the evolution of the Galactic disk are broader topics, and their detailed discussion is beyond the scope of this paper. Several studies with large samples have been dedicated to the AMR in the Galactic disk, including Feltzing et al. (2001), Lin et al. (2020), Sahlholdt et al. (2022), and Patil et al. (2023), to name a few.

4.2. Abundance trend with age

The distributions of $[\text{Mg}/\text{Fe}]$, $[\text{Y}/\text{Fe}]$, and $[\text{Y}/\text{Mg}]$ with respect to stellar ages of the combined sample are shown in Fig. 3. As we see from the $[\text{Mg}/\text{Fe}]$ – $[\text{Fe}/\text{H}]$ distribution (Fig. 1), the thin and thick disk objects show a clear dichotomy in the $[\text{Mg}/\text{Fe}]$ –age plane as well. The $[\text{Mg}/\text{Fe}]$ and $[\text{Y}/\text{Fe}]$ ratios show positive and negative slopes, respectively, with respect to age, as expected from their origin and chemical evolution models. Mg is an α -element produced by Type II supernovae (SNe II) on a shorter timescale ($\leq 10^7$ yrs; e.g. Kobayashi et al. 2006). SNe II were the main contributors of metals to the interstellar medium during the early stages of the chemical evolution. So, α -elements show a positive trend with respect to age. Y is an s-process element produced in low- and intermediate-mass asymptotic giant branch stars, which contributed to the chemical evolution much later compared to SNe II. As a result, Y shows a negative trend with stellar ages (Nomoto et al. 2013; Matteucci 2014; Karakas & Lattanzio 2014; Spina et al. 2016 and references therein).

As a consequence of different origins and chemical evolution, the $[\text{Y}/\text{Mg}]$ ratio has a steeper dependence on stellar ages. As seen from Fig. 3 (bottom panel), the $[\text{Y}/\text{Mg}]$ ratio of our sample shows a strong anti-correlation with age. The scatter in the $[\text{Y}/\text{Mg}]$ ratio of our sample is small compared to that found in other samples of solar-type stars in the literature (e.g. Feltzing et al. 2017; Titarenko et al. 2019; Casali et al. 2020). We note continuity in the $[\text{Y}/\text{Mg}]$ –age correlation between the thin and thick disk stars. We also note that there is no significant gradient of $[\text{Y}/\text{Mg}]$ with respect to $[\text{Fe}/\text{H}]$, as was seen in Feltzing et al. (2017).

4.3. The $[\text{Y}/\text{Mg}]$ chemical clock

In this section we analyse the $[\text{Y}/\text{Mg}]$ –age correlation in our sample. The stellar ages derived from isochrone fitting were used in this analysis. We performed a simple linear regression fitting to derive the empirical relation connecting the $[\text{Y}/\text{Mg}]$ ratio and

⁶ Chemically defined

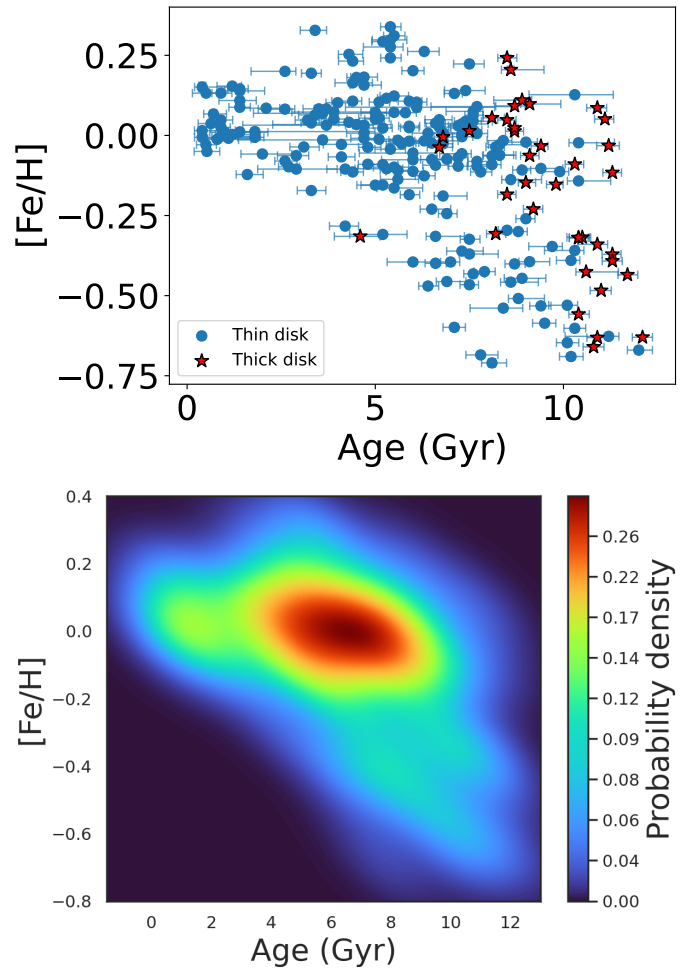
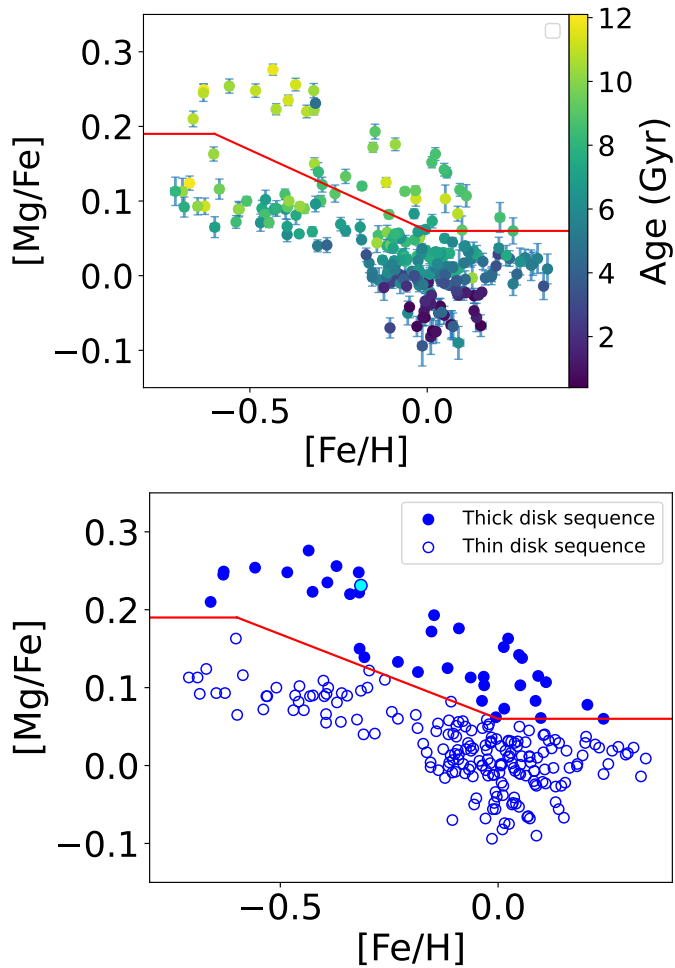


Fig. 1: [Mg/Fe] ratio as a function of [Fe/H] for the combined sample. The solid red line shows the separation between thin and thick disk stars based on the [Mg/Fe] ratio, similar to Adibekyan et al. (2011): [Mg/Fe] = +0.19 for [Fe/H] ≤ −0.6, [Mg/Fe] = −0.217 × [Fe/H] + 0.06 for −0.6 < [Fe/H] ≤ 0, and [Mg/Fe] = +0.06 for [Fe/H] > 0. Stars above this line belong to the Galactic thick disk. The cyan circle is the anomalous star HD 65907.

stellar ages, of the form [Y/Mg] = a × Age + b. From the linear fitting, we find that the [Y/Mg] of the sample is correlated to the stellar age through the relation (Fig. 4)

$$[Y/Mg] = -0.040(\pm 0.001) \times \text{Age (Gyr)} + 0.186(\pm 0.036). \quad (2)$$

To get the best possible relation, we eliminated a few stars that lie outside the bulk of the sample in the [Y/Mg]–age space. The outlier limit is set at the 2σ level of the trend (Eq. 2), which is given by the linear function [Y/Mg] = −0.040 × Age (Gyr) + 0.356, as shown in Fig. 4. We also excluded the anomalous star HD 65907 from this analysis. We did not make any distinction between the thin and thick disk objects. From the linear fit shown in Fig. 5 for the sample after excluding the outliers, we obtained a relation of the form

$$[Y/Mg] = -0.041(\pm 0.001) \times \text{Age (Gyr)} + 0.187(\pm 0.040). \quad (3)$$

However, from the analysis of a sample of 714 solar-type stars, Feltzing et al. (2017) first identified the metallicity dependence of the [Y/Mg] chemical clock, which was subsequently found in the samples of Delgado Mena et al. (2019) and Casali

Fig. 2: AMD of the sample. The red star that is far from the other thick disk objects in the upper panel is the anomalous star HD 65907. The bottom panel is the density plot for the AMD of the sample.

et al. (2020). To verify the metallicity dependence of Eq. 3, we examined the distribution of [Y/Mg] residuals ($\Delta[Y/Mg] = [Y/Mg]_{\text{obs}} - [Y/Mg]_{\text{pred}}$) with respect to metallicity to see if there exist any trend. As we can see from Fig. 6, the $\Delta[Y/Mg]$ is independent of metallicity up to a value of [Fe/H] ~ −0.17 and show a trend below that. This confirms that the [Y/Mg] chemical clock depends on the metallicity and that the whole sample cannot be represented using the single relation given in Eq. 3. Hence, we divided the sample into two metallicity bins, $-0.71 \leq [\text{Fe}/\text{H}] < -0.17$ and $-0.17 \leq [\text{Fe}/\text{H}] < +0.34$, and performed the fitting separately, as shown in Fig. 7. This simple linear fitting resulted in the following relations:

$$\begin{aligned} [Y/Mg] &= -0.0362(\pm 0.0004) \times \text{Age (Gyr)} + 0.0867(\pm 0.0285); \\ &\quad (\text{for } -0.71 \leq [\text{Fe}/\text{H}] < -0.17) \\ [Y/Mg] &= -0.0340(\pm 0.0006) \times \text{Age (Gyr)} + 0.1656(\pm 0.0346); \\ &\quad (\text{for } -0.17 \leq [\text{Fe}/\text{H}] < +0.34). \end{aligned} \quad (4)$$

We performed this fitting for five different metallicity bins of width 0.2 dex as well, and note that the results do not produce significant deviations from the results obtained using Eq. 4.

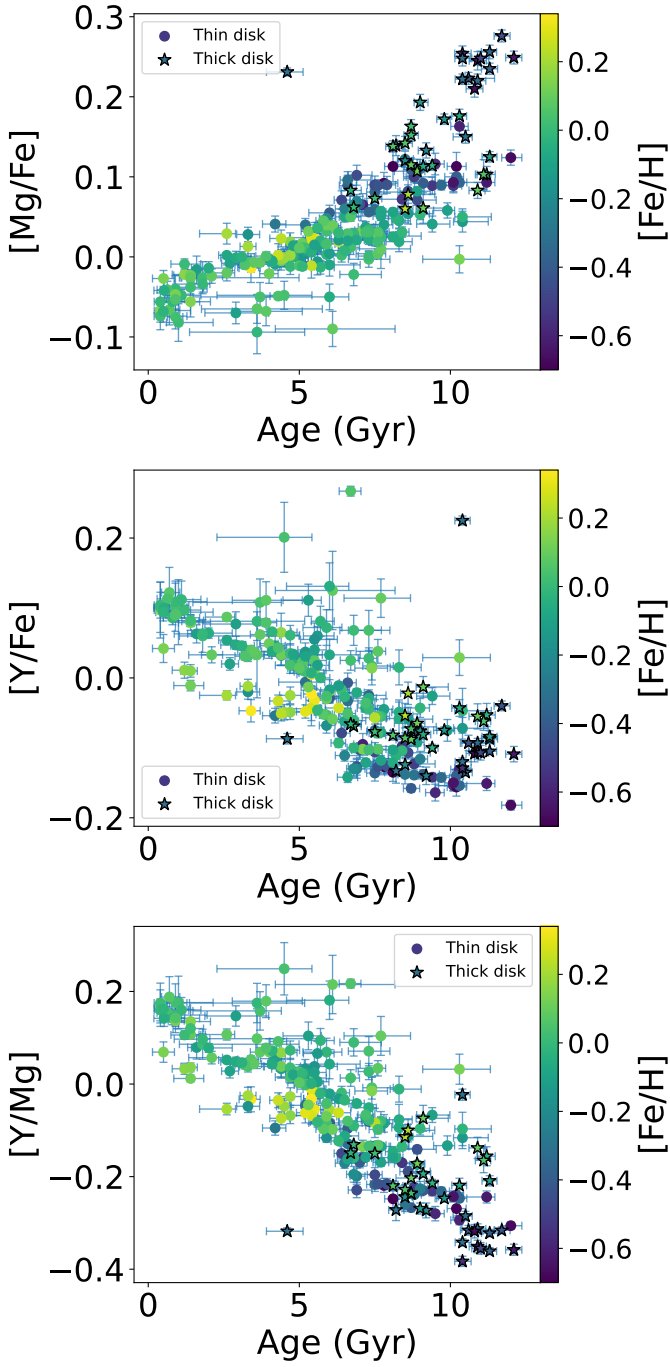


Fig. 3: [Mg/Fe], [Y/Fe], and [Y/Mg] ratios as a function of age for the combined sample, colour-coded by [Fe/H]. The star at ~ 5 Gyr is HD 65907 and is probably the result of a former mass-transfer event.

We then inverted the relations in Eq. 4 to get the stellar dating relations of the form

$$\text{Age (Gyr)} = -27.6243(\pm 0.3053) \times [\text{Y/Mg}] + 2.3950(\pm 0.8139);$$

(for $-0.71 \leq [\text{Fe}/\text{H}] < -0.17$)

$$\text{Age (Gyr)} = -29.4118(\pm 0.5191) \times [\text{Y/Mg}] + 4.8706(\pm 1.1039);$$

(for $-0.17 \leq [\text{Fe}/\text{H}] < +0.34$).

(5)

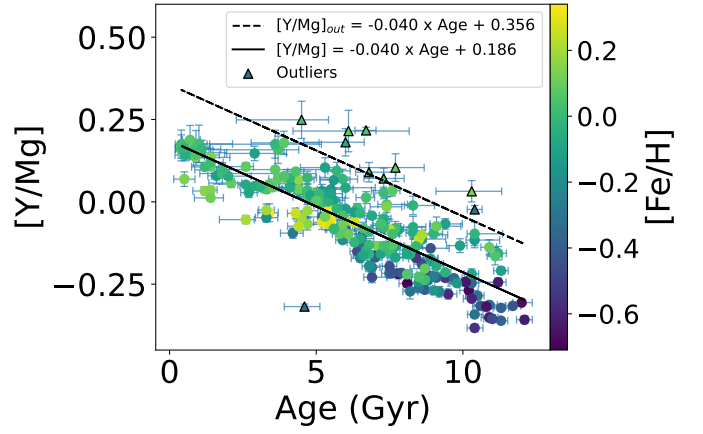


Fig. 4: Linear fit to the [Y/Mg]–age distribution of the whole sample (solid black line) and the outlier cut (dashed black line). The outlier limit is set at the 2σ level of the trend. The triangle in the lower part of the plot is the anomalous star HD 65907.

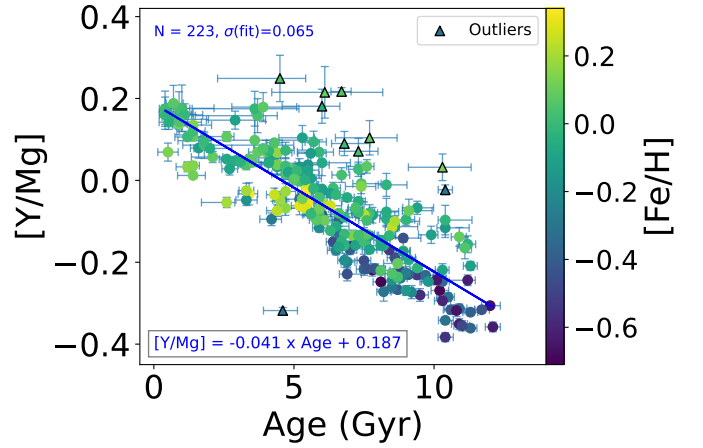


Fig. 5: Best linear fit (solid blue line) for the [Y/Mg]–age distribution of the sample. The fitting function is described in the text (Eq. 3).

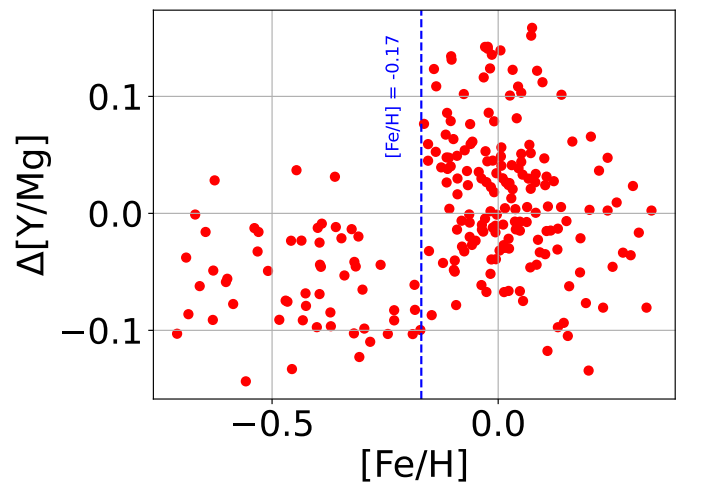


Fig. 6: Distribution of the [Y/Mg] residuals ($\Delta[\text{Y/Mg}]$) with respect to the metallicity of the sample. The vertical dashed line at $[\text{Fe}/\text{H}] = -0.17$ represents the point below which $\Delta[\text{Y/Mg}]$ shows an offset with metallicity.

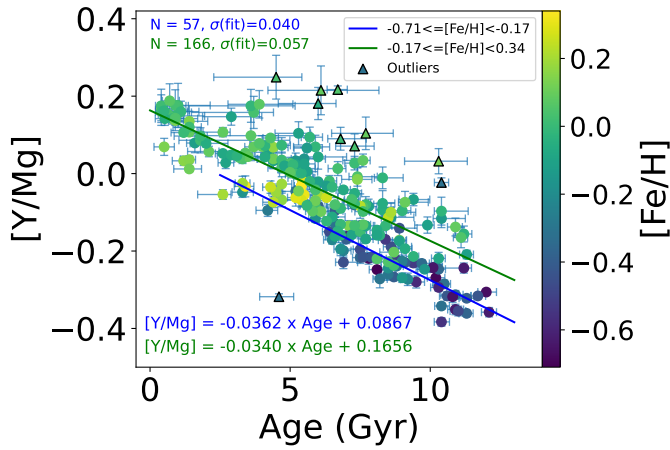


Fig. 7: [Y/Mg]–age linear fits for the sample in two metallicity bins: $-0.71 \leq [\text{Fe}/\text{H}] < -0.17$ (solid blue line) and $-0.17 \leq [\text{Fe}/\text{H}] < +0.34$ (solid green line).

Since we identified the metallicity dependence of the [Y/Mg] ratio in the sample, we also performed a multivariate (MV) linear regression fitting by incorporating the [Fe/H] as well. The obtained relation as a function of stellar age and metallicity is given by

$$[\text{Y}/\text{Mg}] = -0.036(\pm 0.001) \times \text{Age (Gyr)} + 0.125(\pm 0.010) \times [\text{Fe}/\text{H}] + 0.165(\pm 0.034). \quad (6)$$

The chemical age is given by the relation

$$\text{Age (Gyr)} = -27.701(\pm 0.461) \times [\text{Y}/\text{Mg}] + 3.454(\pm 0.329) \times [\text{Fe}/\text{H}] + 4.576(\pm 1.013). \quad (7)$$

Figure 8 shows the relation in Eq. 6 for three different metallicity values, $[\text{Fe}/\text{H}] = -0.5, -0.1,$ and $+0.3$.

The chemical ages of the sample are calculated using both Eq. 5 and Eq. 7 and compared with the isochrone ages and with each other. The chemical ages do not show any trend with the isochrone ages (offset ~ 0). The standard deviation (SD) of the single variate (SV) chemical age (Eq. 5) with respect to the isochrone age is 1.55 Gyr and that of the MV chemical age (Eq. 7) is 1.66 Gyr. We note that the average uncertainty in the isochrone ages of the sample is ~ 0.4 Gyr. From the comparison between the SV and MV chemical ages shown in Fig. 9, we see that the two ages match quite well, with an offset of only -0.005 Gyr. The mean scatter and SD between them are 0.50 and 0.62 Gyr, respectively.

4.3.1. Validation using open clusters and stars with asteroseismic ages

To validate our relations in Eqs. 5 and 7, we used the data for open clusters (OCs) and stars with asteroseismic ages. OCs are one of the powerful tools for validating the chemical clocks because the member stars of each cluster show homogeneity in age and chemical composition. As a result, their ages have been precisely determined through isochrone fitting from the observation of several member stars (e.g. Casali et al. 2019; Viscasillas Vázquez et al. 2022). Casali et al. (2020) present a list of OCs selected from the iDR5 (fifth internal data release) of the GES (Gilmore et al. 2012; Randich et al. 2013), with cluster membership probability of at least 80%. From this list, we selected 13 OCs with $R_{GC} \geq 6.5$ kpc.

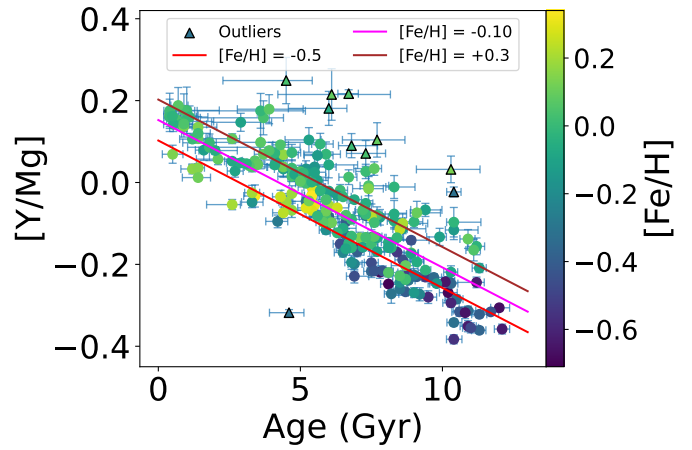


Fig. 8: MV linear fits for the [Y/Mg]–age distribution of the sample for three different metallicities. The fitting function is described in the text (Eq. 6).

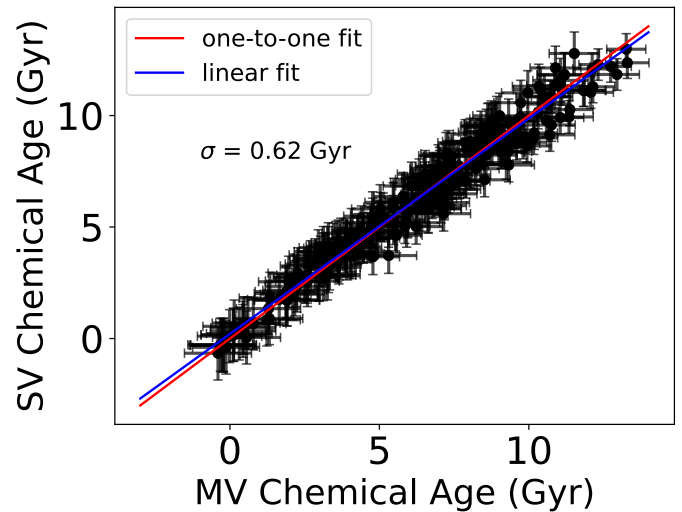


Fig. 9: Correlation between the SV (Eq. 5) and MV (Eq. 7) chemical ages of the stellar sample.

In the case of single stars, asteroseismology provides the reliable ages from the solar-like oscillations on the stellar surface (Chaplin & Miglio 2013; Silva Aguirre et al. 2012; Christensen-Dalsgaard 2016). Silva Aguirre et al. (2017) present the asteroseismic ages for a sample of 66 main-sequence stars from the *Kepler* LEGACY sample (KLS) based on the asteroseismic data from the *Kepler* mission. The KLS is claimed to have the best asteroseismic data available for solar-like stars. We selected ten stars from the KLS for which the precise abundances are available in the literature. The validation sample of OCs and KLS stars used to calibrate our chemical clocks are given in Table 1. The Y and Mg abundances of OCs and KLS stars are adopted from Casali et al. (2020) and Nissen et al. (2017), respectively.

Figure 10 shows the comparisons of the SV (upper panel) and MV (middle panel) chemical ages of the validation sample calculated using our relations with their literature ages. The lower panel of this figure shows the correlation between the SV and MV chemical ages of this sample. As can be seen from the figure, the OCs show a larger scatter compared to the KLS stars, but both agree with the [Y/Mg] clock within 1σ or 2σ .

This may be because these cluster members are giants or subgiants, whereas our relations are derived based on a sample of dwarf stars. In addition to this, even though the OCs in the inner Galactic disk ($R_{GC} < 6.5$ kpc) are excluded from our comparison, some of them could have originally belonged to this region and may currently be in the solar neighbourhood as a result of radial migration (e.g. [Viscassillas Vázquez et al. 2022](#)). Since our stellar sample lies in the solar neighbourhood, this also may have contributed to the scatter seen in Fig. 10.

Single variate chemical clock (Eq. 5): In the case of KLS stars with asteroseismic ages, the mean scatter (accuracy) of this chemical clock is 0.91 Gyr, with a SD (i.e. precision) of 0.96 Gyr and a mean relative error (MRE)⁷ of 38%. The average uncertainty in the seismic ages of the sample is ~ 0.52 Gyr, and the [Y/Mg] has a mean error of 0.013 dex, which translates to ~ 0.32 Gyr. By incorporating these two errors in to the mean scatter, the actual accuracy of the SV chemical age is estimated to be ~ 0.67 Gyr for the KLS stars. In the case of OCs, the mean scatter and the SD of the SV chemical clock are 1.10 and 1.24 Gyr, respectively. The average uncertainty in their isochrone ages is 0.23 Gyr and that from the [Y/Mg] ratio is 0.73 Gyr ($\equiv 0.03$ dex). Subtracting these errors results in an accuracy of 0.79 Gyr in the SV chemical ages of the OCs.

Multivariate chemical clock (Eq. 7): The mean scatter and the SD are 0.76 Gyr and 0.99 Gyr, respectively, with a MRE of 33% for the KLS stars. In the case of OCs, the mean scatter and the SD for this chemical clock are 1.17 Gyr and 1.45 Gyr, respectively. Incorporating the uncertainties in the literature ages and the [Y/Mg] ratios, the accuracy of the MV chemical ages is estimated to be 0.45 Gyr and 0.88 Gyr, respectively, for the KLS stars and the OCs.

In summary, the accuracy we have obtained using our chemical clocks based on the KLS stars with asteroseismic ages and the OCs with isochrone ages respectively are ~ 0.67 and 0.79 Gyr (SV chemical age) and ~ 0.45 and 0.88 Gyr (MV chemical age). These values are similar to the accuracy achieved for the solar twin stars in the solar neighbourhood ($\sim 0.8 - 1$ Gyr; [Nissen 2015, 2016](#); [Tucci Maia et al. 2016](#); [Spina et al. 2018](#)). Since the KLS stars are dwarfs and lie in the close vicinity of the Sun as our stellar sample, the validation using them is likely more accurate compared to the OCs.

4.3.2. Chemical clock in the thin and thick disks

While the studies using solar twins, analogues, and solar-type stars with $[\text{Fe}/\text{H}] \geq -0.3$ confirmed the tight correlation between the [Y/Mg] ratio and stellar ages irrespective of the population (thin or thick disk; [Nissen 2016](#); [Tucci Maia et al. 2016](#); [Spina et al. 2016, 2018](#); [Nissen et al. 2017, 2020](#); [Jofré et al. 2020](#)), a few recent studies have suggested that the [Y/Mg] chemical clock can only be used for thin disk stars and may not be valid for lower metallicities or thick disk stars (e.g. [Feltzing et al. 2017](#); [Delgado Mena et al. 2018, 2019](#); [Titarenko et al. 2019](#); [Tautvaišienė et al. 2021](#)). [Feltzing et al. \(2017\)](#) suggest that the [Y/Mg] - age distribution is almost flat and has no predictive power on age for $[\text{Fe}/\text{H}] < -0.5$. However, [Delgado Mena et al. \(2018\)](#) show that it still has a correlation with age (up to $[\text{Fe}/\text{H}] \sim -0.8$), but only for thin disk stars. The trend becomes flat for thick disk stars, and for thin disk stars with ages ≥ 8 Gyr. From an AMBRE (Archéologie avec Matisse Basée sur les Archives de l'ESO) sample of solar-type stars, [Titarenko et al. \(2019\)](#) identified different slopes for thin disk and thick disk stars

with the thick disk stars showing a steeper dependence. Recently, [Tautvaišienė et al. \(2021\)](#) found that thick disk stars (233 stars including dwarfs and giants) show no trend of [Y/Mg] with age (slope ~ -0.002), contrarily to the slopes identified for the thick disk stars of [Titarenko et al. \(2019\)](#) and [Bensby et al. \(2014\)](#). This may be due to the different luminosity classes in their sample.

We examined the dependence of the [Y/Mg] chemical clock on stellar age for the thin and thick disk stars separately and found that both components show almost the same correlation, with slopes $-0.039(\pm 0.001)$ and $-0.034(\pm 0.001)$, respectively. The linear fits (Eq. 8) for the two populations are shown in Fig. 11.

$$\begin{aligned} [\text{Y}/\text{Mg}]_{\text{Thin}} &= -0.039(\pm 0.001) \times \text{Age (Gyr)} + 0.178(\pm 0.038) \\ [\text{Y}/\text{Mg}]_{\text{Thick}} &= -0.034(\pm 0.001) \times \text{Age (Gyr)} + 0.089(\pm 0.015). \end{aligned} \quad (8)$$

Our results disagree with previous studies, which found that the thick disk stars showed either no trend at all or a different trend than the thin disk stars. In particular, the thick disk stars in [Spina et al. \(2018\)](#) seem to have a small offset relative to the [Y/Mg]-age relation defined by their thin disk sample. However, their sample of thick disk stars is relatively small, making it difficult to perform a separate fit for the [Y/Mg]-age relation of the thick disk. Although our sample size of thick disk stars has increased relative to the study of [Spina et al. \(2018\)](#), we have to keep in mind that our number is still relatively small (36 objects without outliers). We note that the results may be somewhat biased due to the selection biases of thick and thin disk stars in different studies.

4.3.3. Comparison with previous works

The slopes of the [Y/Mg]-age distribution for solar twins and solar-type stars from different studies, along with our estimates, are given in Table 2. These estimates are based on the linear relation between [Y/Mg] and the stellar ages. We note that, while the relations obtained for the solar twins by different authors are similar irrespective of the sample size, the solar-type stars give different slopes. However, [Nissen et al. \(2017\)](#), [Delgado Mena et al. \(2019\)](#), [Nissen et al. \(2020\)](#), and [Tautvaišienė et al. \(2021\)](#) show similar values that match those of solar twins. Different samples of solar-type stars listed in Table 2 have different range of metallicities. Hence, the difference in the slopes plausibly results from the metallicity dependence, as discussed in [Feltzing et al. \(2017\)](#) and [Delgado Mena et al. \(2018, 2019\)](#). However, when we consider the sample irrespective of the population, our relations are compatible with those found for the solar twins by [Nissen \(2016\)](#) and for solar-type stars by [Nissen et al. \(2017, 2020\)](#). While our estimate for the thick disk stars matches the estimate of [Tautvaišienė et al. \(2021\)](#) from a sample of 76 thick disk giants, it disagrees with other samples of thick disk stars.

The values listed in Table 2 are based on a simple linear regression fit between the chemical clock and the stellar ages. In light of the results from [Feltzing et al. \(2017\)](#) and [Delgado Mena et al. \(2018\)](#), and the non-universality of the chemical clock - age relation in the Galactic disk ([Casali et al. 2020](#)), a few recent studies have attempted to perform multiple variable linear regression fitting by including, for example, the stellar atmospheric parameters, Galactocentric distances, and stellar masses, in addition to the stellar ages ([Delgado Mena et al. 2019](#); [Casali et al. 2020](#); [Viscassillas Vázquez et al. 2022](#)).

⁷ $\text{RE} = \frac{|\text{Literature age} - \text{Chemical age}|}{\text{Literature age}}$

Table 1: Properties of the OCs and KLS stars used in this study.

ID	[Fe/H] (dex)	[Y/Mg] (dex)	Age (Gyr)	ID	[Fe/H] (dex)	[Y/Mg] (dex)	Age (Gyr)
OCs*				KLS stars [†]			
Berkeley 31	-0.270±0.060	-0.010±0.030	2.50±0.30	KIC 3427720	-0.024±0.017	-0.017±0.015	2.40±0.30
Berkeley 36	-0.160±0.100	-0.050±0.060	7.00±0.50	KIC 6106415	-0.037±0.012	0.002±0.011	4.80±0.60
Berkeley 44	0.270±0.060	0.140±0.070	1.60±0.30	KIC 6225718	-0.110±0.014	0.051±0.012	2.60±0.40
M 67	-0.010±0.040	0.000±0.010	4.30±0.50	KIC 7940546	-0.126±0.012	0.056±0.010	2.40±0.30
Melotte 71	-0.090±0.030	0.070±0.010	0.83±0.18	KIC 9139151	0.096±0.019	0.101±0.017	1.90±0.70
NGC 2243	-0.380±0.040	-0.040±0.030	4.00±1.20	KIC 10162436	-0.073±0.021	0.071±0.017	2.50±0.40
NGC 2420	-0.130±0.040	0.070±0.030	2.20±0.30	KIC 10644253	0.130±0.019	0.066±0.017	1.30±0.70
NGC 4815	0.110±0.010	0.110±0.090	0.57±0.07	KIC 12069424	0.093±0.007	-0.090±0.009	7.00±0.50
NGC 6067	0.200±0.080	0.080±0.040	0.10±0.05	KIC 12069449	0.062±0.007	-0.085±0.009	7.10±0.50
NGC 6633	-0.010±0.110	0.080±0.020	0.52±0.10	KIC 12258514	0.027±0.007	-0.051±0.016	4.50±0.80
NGC 6802	0.100±0.020	0.170±0.020	1.00±0.10				
Pismis 18	0.220±0.040	0.050±0.040	1.20±0.04				
Trumpler 20	0.150±0.070	0.120±0.020	1.50±0.15				

References: * Casali et al. (2020) and references therein, [†] Nissen et al. (2017) and references therein

The accuracy and precision of the [Y/Mg] chemical clock when considered as a function of age, [Fe/H], and R_{GC} are 1.6 Gyr and 2.8 Gyr, respectively (Viscasillas Vázquez et al. 2022). Delgado Mena et al. (2019) were able to determine the ages with a precision of 1.85 Gyr and MRE~57% using their 1D [Y/Mg] chemical clock. When using 2D relations, including $T_{eff}/[Fe/H]/mass$ as well, they got precisions and MRE (1.57 Gyr, 48%), (1.73 Gyr, 40%), and (1.71 Gyr, 37%), respectively, whereas their 3D relations (T_{eff} and [Fe/H] along with age) resulted in a precision of 1.47 Gyr with an MRE of 51%. The accuracy achieved by Titarenko et al. (2019) using their 1D dating relation is 2 Gyr. Meanwhile, the accuracy and precision of the chemical ages calculated using our relation (Eq. 7) are ~0.45 Gyr and 0.99 Gyr, respectively, with a MRE of 33%. Since our sample lies in the solar neighbourhood, we have only discussed the results valid in this region.

5. Conclusions

Based on high-resolution and high-quality HARPS spectra, we estimated the precise stellar atmospheric parameters and chemical abundances of Mg and Y through a line-by-line differential analysis for a sample of 48 metal-poor solar-type stars in the solar neighbourhood. Through the isochrone fitting method, the stellar masses and ages of the sample were also estimated. We performed a joint analysis of these 48 objects, together with 185 solar twins and analogues from our previous studies. The combined sample consists of 233 solar-type stars in the solar neighbourhood with metallicities in the range $-0.71 \leq [Fe/H] < +0.34$. The main results of our homogeneous analysis are summarised as follows:

- The sample shows a clear bimodality in the [Mg/Fe]–[Fe/H] plane, and the thin and thick disk populations are clearly distinguishable. Thick disk stars show higher $[\alpha/Fe]$ values compared to thin disk stars. While the thick disk stars are older than 8 Gyr, the thin disk shows an age spread. Nonetheless, there is no age discontinuity between the two populations.
- Our chemically defined thick disk and thin disk stars overlap in the kinematic space, a behaviour already noted in several previous studies.

- The thick disk stars show an AMR; however, the age and metallicity exhibit an essentially flat distribution and are uncorrelated for the thin disk stars. On the other hand, the two populations blend together in the age–[Fe/H] distribution.
- There exists a correlation between [Mg/Fe] and stellar ages for both populations. However, in the case of [Y/Fe], only the thin disk stars show a correlation. We note a clear dichotomy between these two populations in the [Mg/Fe]–age distribution, whereas there is no separation between them in the [Y/Fe]–age space.
- The [Y/Mg] ratio shows a strong anti-correlation with stellar age. Our analysis confirms the metallicity dependence of the [Y/Mg] chemical clock. We note the scatter in our [Y/Mg]–age distribution is lower than that of all previous studies of solar-type stars. There is no discontinuity between the thin and thick disks in the [Y/Mg]–age correlation. Our estimates of the slope are compatible with those found for solar twins and other samples of solar-type stars in the higher metallicity bin ($[Fe/H] > -0.30$).
- For the first time in the literature, we report similar slopes of the [Y/Mg]–age correlation for thin (–0.039) and thick disk (–0.034) stars.
- Using the dating relations (Eqs. 5 and 7), we achieve high accuracies (0.67 and 0.45 Gyr, respectively) and precisions (0.96 and 0.99 Gyr, respectively). These accuracies are compatible with the best accuracy achieved for solar twins to date (~0.8 - 1.0 Gyr) in the solar neighbourhood. The MREs in the chemical ages using these relations are 38% and 33%, respectively. The chemical clock based on the MV relation (Eq. 7) performs somewhat better than the SV relations in two metallicity regimes (Eq. 5).

The relations connecting the abundance ratios and stellar ages are related to the chemo-dynamical evolution of the Galaxy and can be used to study different components of it (Haywood et al. 2013, 2016). From our analysis, we find that the [Y/Mg] chemical clock can be used as an age proxy for solar-type stars. The empirical relations showcased in this work should be used only for stars in the solar neighbourhood and in the same parameter range as our sample. The high-precision outcomes of our work are expected to provide contributions to the understanding of different populations of the Galaxy and its chemical evolution.

Table 2: Slopes of the [Y/Mg]–age distribution of stars in the solar neighbourhood.

Slope (dex Gyr ⁻¹)	N [†]	Pop [*]	Ref	Slope (dex Gyr ⁻¹)	N [†]	Pop [*]	[Fe/H]	Ref
solar twins				solar-type				
-0.0404±0.0019	18	Thin disk	Nissen (2015)	-0.0362±0.0004	57		-0.71 - -0.17	This work
-0.0371±0.0013	21		Nissen (2016)	-0.0340±0.0006	166		-0.17 - +0.34	This work
-0.0410±0.0010	65		Tucci Maia et al. (2016)	-0.0390±0.0010	187	Thin disk	-0.71 - +0.34	This work
-0.0410±0.0017	45		Spina et al. (2016)	-0.0340±0.0010	36	Thick disk	-0.71 - +0.05	This work
-0.0460±0.0020	76		Spina et al. (2018)	-0.0347±0.0012	31		-0.15 - +0.15	Nissen et al. (2017)
-0.0420±0.0030	66	Thin disk	Spina et al. (2018)	-0.0199		Thin disk	-0.80 - -0.20	Delgado Mena et al. (2018)
-0.0410±0.0030			Delgado Mena et al. (2019)	-0.0420±0.0010	354		-1.15 - +0.55	Delgado Mena et al. (2019)
-0.0420±0.0030	80		Jofré et al. (2020)	-0.0290±0.0020	22	Thin disk	-0.80 - +0.40	Titarenko et al. (2019)
-0.0400±0.0020			Casali et al. (2020)	-0.0820±0.0020	11	Thick disk	-0.80 - +0.20	Titarenko et al. (2019)
				-0.0383±0.0010	68		-0.30 - +0.30	Nissen et al. (2020)
				-0.0270±0.0030	368	Thin disk	-0.60 - +0.40	Tautvaišienė et al. (2021) [‡]
				-0.0410±0.0130*	76	Thick disk	-0.46±0.12	Tautvaišienė et al. (2021)
				-0.0140±0.0040	66	Thick disk	-1.00 - +0.40	Tautvaišienė et al. (2021) (for Bensby et al. (2014) sample)
				-0.0020±0.0030	233	Thick disk	-1.00 - +0.40	Tautvaišienė et al. (2021) and references therein [‡]

[†] No. of stars used to derive the relation

* Fitting includes both the populations if not mentioned

[‡] Sample includes dwarf and giants

* Only giants

Acknowledgements. JS and JM acknowledge the support from FAPESP (2022/10325-3 and 2018/04055-8). This work made use of the SIMBAD astronomical database, operated at CDS, Strasbourg, France, and the NASA ADS, USA. This work has made use of data from the European Space Agency (ESA) mission *Gaia* (<https://www.cosmos.esa.int/gaia>), processed by the *Gaia* Data Processing and Analysis Consortium (DPAC, <https://www.cosmos.esa.int/web/gaia/dpac/consortium>). Funding for the DPAC has been provided by national institutions, in particular the institutions participating in the *Gaia* Multilateral Agreement. Based on data collected at the European Southern Observatory under ESO programs 60.A-9036(A), 60.A-9700(G), 60.A-9709(G), 072.C-0488(E), 073.C-0733(A), 077.C-0295(A), 077.C-0295(B), 078.C-0209(A), 080.C-0712(A), 082.C-0212(A), 082.C-0212(B), 084.C-0229(A), 085.C-0019(A), 085.C-0063(A), 086.C-0284(A), 087.C-0831(A), 088.C-0323(A), 089.C-0732(A), 091.C-0034(A), 091.C-0936(A), 092.C-0579(A), 092.C-0721(A), 093.C-0409(A), 094.C-0797(A), 096.C-0053(A), 096.C-0210(A), 098.C-0366(A), 106.21TJ.001, 183.C-0972(A), 184.C-0815(A), 184.C-0815(C), 184.C-0815(F), 190.C-0027(A), 192.C-0852(A), 196.C-0042, 196.C-0042(D), 196.C-0042(E), 0100.C-0097(A), 1102.C-0923(A), and 1102.C-0923(C).

References

- Adibekyan, V. Z., Figueira, P., Santos, N. C., et al. 2013, *A&A*, 554, A44
- Adibekyan, V. Z., Santos, N. C., Sousa, S. G., & Israelian, G. 2011, *A&A*, 535, L11
- Adibekyan, V. Z., Sousa, S. G., Santos, N. C., et al. 2012, *A&A*, 545, A32
- Alfredo Collazos, J. 2023, arXiv e-prints, arXiv:2308.08492
- Anders, F., Chiappini, C., Santiago, B. X., et al. 2014, *A&A*, 564, A115
- Babusiaux, C., Fabricius, C., Khanna, S., et al. 2022, arXiv e-prints, arXiv:2206.05989
- Bedell, M., Meléndez, J., Bean, J. L., et al. 2014, *ApJ*, 795, 23
- Bensby, T., Feltzing, S., & Lundström, I. 2003, *A&A*, 410, 527
- Bensby, T., Feltzing, S., Lundström, I., & Ilyin, I. 2005, *A&A*, 433, 185
- Bensby, T., Feltzing, S., & Oey, M. S. 2014, *A&A*, 562, A71
- Bergemann, M., Ruchti, G. R., Serenelli, A., et al. 2014, *A&A*, 565, A89
- Bland-Hawthorn, J. & Gerhard, O. 2016, *ARA&A*, 54, 529
- Bovy, J. 2015, *ApJS*, 216, 29
- Bovy, J., Rix, H.-W., & Hogg, D. W. 2012a, *ApJ*, 751, 131
- Bovy, J., Rix, H.-W., Liu, C., et al. 2012b, *ApJ*, 753, 148
- Castelli, E. & Teixeira, R. 2024, *MNRAS*, 530, 2648
- Casagrande, L., Schönrich, R., Asplund, M., et al. 2011, *A&A*, 530, A138
- Casali, G., Magrini, L., Tognelli, E., et al. 2019, *A&A*, 629, A62
- Casali, G., Spina, L., Magrini, L., et al. 2020, *A&A*, 639, A127
- Casamiquela, L., Soubiran, C., Jofré, P., et al. 2021, *A&A*, 652, A25
- Castelli, F. & Kurucz, R. L. 2003, in *Proceedings of the IAU Symp. No 210, Vol. 210, Modelling of Stellar Atmospheres*, ed. N. Piskunov, W. W. Weiss, & D. F. Gray, A20
- Cayrel de Strobel, G. 1996, *A&A Rev.*, 7, 243
- Chaplin, W. J. & Miglio, A. 2013, *ARA&A*, 51, 353
- Christensen-Dalsgaard, J. 2016, arXiv e-prints, arXiv:1602.06838
- Cox, A. N. 2000, *Allen's astrophysical quantities* (Springer)
- da Silva, R., Porto de Mello, G. F., Milone, A. C., et al. 2012, *A&A*, 542, A84
- Delgado Mena, E., Moya, A., Adibekyan, V., et al. 2019, *A&A*, 624, A78
- Delgado Mena, E., Tsantaki, M., Zh. Adibekyan, V., et al. 2018, in *Astrometry and Astrophysics in the Gaia Sky*, ed. A. Recio-Blanco, P. de Laverny, A. G. A. Brown, & T. Prusti, Vol. 330, 156–159
- Edvardsson, B., Andersen, J., Gustafsson, B., et al. 1993, *A&A*, 275, 101
- Epstein, C. R., Johnson, J. A., Dong, S., et al. 2010, *ApJ*, 709, 447
- Feltzing, S., Holmberg, J., & Hurley, J. R. 2001, *A&A*, 377, 911
- Feltzing, S., Howes, L. M., McMillan, P. J., & Stenker, E. 2017, *MNRAS*, 465, L109
- Fuhrmann, K. 1998, *A&A*, 338, 161
- Fuhrmann, K., Chini, R., Haas, M., et al. 2012, *ApJ*, 761, 159
- Gaia Collaboration, Prusti, T., de Bruijne, J. H. J., et al. 2016, *A&A*, 595, A1
- Gaia Collaboration, Vallenari, A., Brown, A. G. A., et al. 2022, arXiv e-prints, arXiv:2208.00211
- Gent, M. R., Eitner, P., Serenelli, A., et al. 2024, *A&A*, 683, A74
- Gilmore, G., Randich, S., Asplund, M., et al. 2012, *The Messenger*, 147, 25
- Haywood, M. 2006, *MNRAS*, 371, 1760
- Haywood, M. 2008, *A&A*, 482, 673
- Haywood, M., Di Matteo, P., Lehnert, M. D., Katz, D., & Gómez, A. 2013, *A&A*, 560, A109

- Haywood, M., Lehnert, M. D., Di Matteo, P., et al. 2016, *A&A*, 589, A66
- Howes, L. M., Lindegren, L., Feltzing, S., Church, R. P., & Bensby, T. 2019, *A&A*, 622, A27
- Imig, J., Price, C., Holtzman, J. A., et al. 2023, *ApJ*, 954, 124
- Jofré, P., Jackson, H., & Tucci Maia, M. 2020, *A&A*, 633, L9
- Karakas, A. I. & Lattanzio, J. C. 2014, *PASA*, 31, e030
- Kim, Y.-C., Demarque, P., Yi, S. K., & Alexander, D. R. 2002, *ApJS*, 143, 499
- Kobayashi, C., Umeda, H., Nomoto, K., Tominaga, N., & Ohkubo, T. 2006, *ApJ*, 653, 1145
- Lee, Y. S., Beers, T. C., An, D., et al. 2011, *ApJ*, 738, 187
- Leung, H. W., Bovy, J., Mackereth, J. T., & Miglio, A. 2023, *MNRAS*, 522, 4577
- Li, Q.-D., Wang, H.-F., Luo, Y.-P., et al. 2022, *ApJS*, 262, 20
- Lin, J., Asplund, M., Ting, Y.-S., et al. 2020, *MNRAS*, 491, 2043
- Liu, C. & van de Ven, G. 2012, *MNRAS*, 425, 2144
- Martos, G., Meléndez, J., Rathsam, A., & Carvalho Silva, G. 2023, *MNRAS*, 522, 3217
- Matteucci, F. 2014, in *Saas-Fee Advanced Course*, Vol. 37, *Saas-Fee Advanced Course*, ed. J. Bland-Hawthorn, K. Freeman, & F. Matteucci, 145
- Meléndez, J., Bergemann, M., Cohen, J. G., et al. 2012, *A&A*, 543, A29
- Meléndez, J., Casagrande, L., Ramírez, I., Asplund, M., & Schuster, W. J. 2010, *A&A*, 515, L3
- Meléndez, J., Dodds-Eden, K., & Robles, J. A. 2006, *ApJ*, 641, L133
- Meléndez, J., Ramírez, I., Karakas, A. I., et al. 2014, *ApJ*, 791, 14
- Moya, A., Sarro, L. M., Delgado-Mena, E., et al. 2022, *A&A*, 660, A15
- Navarro, J. F., Abadi, M. G., Venn, K. A., Freeman, K. C., & Anguiano, B. 2011, *MNRAS*, 412, 1203
- Ness, M. K., Johnston, K. V., Blancato, K., et al. 2019, *ApJ*, 883, 177
- Nidever, D. L., Bovy, J., Bird, J. C., et al. 2014, *ApJ*, 796, 38
- Nissen, P. E. 2015, *A&A*, 579, A52
- Nissen, P. E. 2016, *A&A*, 593, A65
- Nissen, P. E., Christensen-Dalsgaard, J., Mosumgaard, J. R., et al. 2020, *A&A*, 640, A81
- Nissen, P. E., Silva Aguirre, V., Christensen-Dalsgaard, J., et al. 2017, *A&A*, 608, A112
- Nomoto, K., Kobayashi, C., & Tominaga, N. 2013, *ARA&A*, 51, 457
- Patil, A. A., Bovy, J., Jaimungal, S., Frankel, N., & Leung, H. W. 2023, *MNRAS*, 526, 1997
- Ramírez, I. & Meléndez, J. 2005, *ApJ*, 626, 446
- Ramírez, I., Meléndez, J., & Asplund, M. 2009, *A&A*, 508, L17
- Ramírez, I., Meléndez, J., Bean, J., et al. 2014, *A&A*, 572, A48
- Randich, S., Gilmore, G., & Gaia-ESO Consortium. 2013, *The Messenger*, 154, 47
- Rathsam, A., Meléndez, J., & Carvalho Silva, G. 2023, *MNRAS*, 525, 4642
- Reddy, B. E., Lambert, D. L., & Allende Prieto, C. 2006, *MNRAS*, 367, 1329
- Rix, H.-W. & Bovy, J. 2013, *A&A Rev.*, 21, 61
- Sahlholdt, C. L., Feltzing, S., & Feuillet, D. K. 2022, *MNRAS*, 510, 4669
- Salaris, M., Chieffi, A., & Straniero, O. 1993, *ApJ*, 414, 580
- Schirbel, L., Meléndez, J., Karakas, A. I., et al. 2015, *A&A*, 584, A116
- Schönrich, R. & Binney, J. 2009, *MNRAS*, 396, 203
- Schönrich, R., Binney, J., & Dehnen, W. 2010, *MNRAS*, 403, 1829
- Schuster, W. J., Moitinho, A., Márquez, A., Parrao, L., & Covarrubias, E. 2006, *A&A*, 445, 939
- Shejeelammal, J. & Goswami, A. 2024, *MNRAS*, 527, 2323
- Silva Aguirre, V., Casagrande, L., Basu, S., et al. 2012, *ApJ*, 757, 99
- Silva Aguirre, V., Lund, M. N., Antia, H. M., et al. 2017, *ApJ*, 835, 173
- Skúladóttir, Á., Hansen, C. J., Salvadori, S., & Choplin, A. 2019, *A&A*, 631, A171
- Slumstrup, D., Grundahl, F., Brogaard, K., et al. 2017, *A&A*, 604, L8
- Snedden, C., Bean, J., Ivans, I., Lucatello, S., & Sobeck, J. 2012, *MOOG: LTE line analysis and spectrum synthesis*, *Astrophysics Source Code Library*, record ascl:1202.009
- Snedden, C. A. 1973, PhD thesis, THE UNIVERSITY OF TEXAS AT AUSTIN.
- Soderblom, D. R. 2010, *ARA&A*, 48, 581
- Soderblom, D. R. & King, J. R. 1998, in *Solar Analogs: Characteristics and Optimum Candidates.*, ed. J. C. Hall, 41
- Spina, L., Meléndez, J., Karakas, A. I., et al. 2018, *MNRAS*, 474, 2580
- Spina, L., Meléndez, J., Karakas, A. I., et al. 2016, *A&A*, 593, A125
- Tautvaišienė, G., Viscasillas Vázquez, C., Mikolaitis, Š., et al. 2021, *A&A*, 649, A126
- Titarenko, A., Recio-Blanco, A., de Laverny, P., Hayden, M., & Guiglion, G. 2019, *A&A*, 622, A59
- Tucci Maia, M., Ramírez, I., Meléndez, J., et al. 2016, *A&A*, 590, A32
- Viscasillas Vázquez, C., Magrini, L., Casali, G., et al. 2022, *A&A*, 660, A135
- Wang, H.-F., Carraro, G., Li, X., et al. 2024, *ApJ*, 967, 37
- Weinberg, D. H., Holtzman, J. A., Hasselquist, S., et al. 2019, *ApJ*, 874, 102
- Xiang, M. & Rix, H.-W. 2022, *Nature*, 603, 599
- Yana Galarza, J., Meléndez, J., Ramírez, I., et al. 2016, *A&A*, 589, A17
- Yanny, B., Rockosi, C., Newberg, H. J., et al. 2009, *AJ*, 137, 4377
- Yi, S., Demarque, P., Kim, Y.-C., et al. 2001, *ApJS*, 136, 417

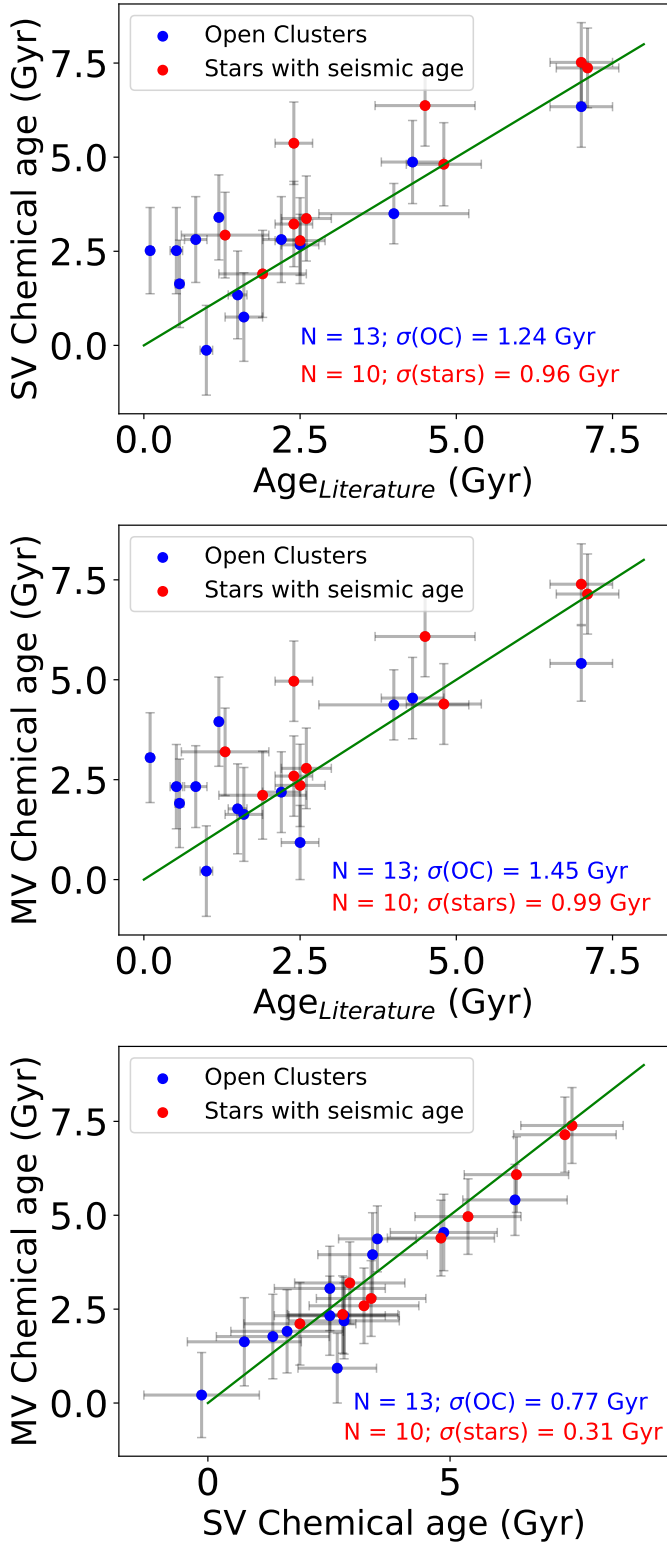


Fig. 10: Comparison of the literature ages of the OCs and KLS stars with their SV (upper panel) and MV (middle panel) chemical ages. The bottom panel shows the correlation between the two chemical ages. The green line represents the one-to-one fit.

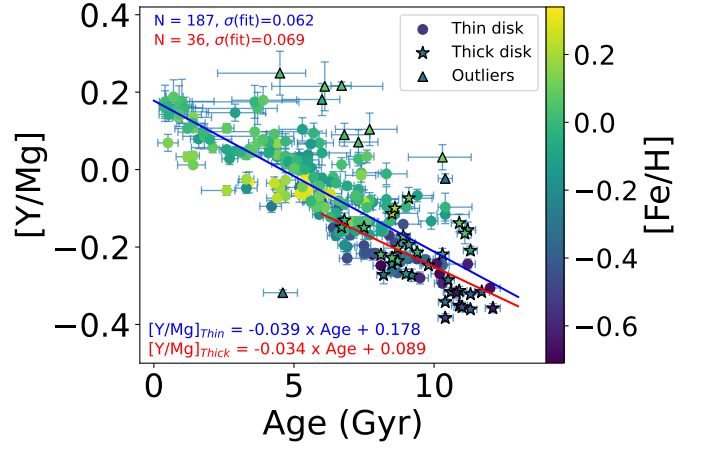


Fig. 11: Best linear fits for thin disk stars (solid blue line) and the thick disk stars (solid red line). The fitting functions are described in the text (Eq. 8).

Appendix A: Stellar atmospheric parameters, mass, age, and elemental abundance ratios

Table A.1: Stellar atmospheric parameters, mass, age, and the elemental abundance ratios of the sample analysed in this study.

HD	HIP	T_{eff} (K)	log g (dex)	[Fe/H] (dex)	ζ (km s ⁻¹)	Age (Gyr)	Mass (M_{\odot})	[Mg/Fe] (dex)	[Y/Fe] (dex)	[Y/Mg] (dex)
208	569	5929±7	4.45±0.02	-0.324±0.006	1.25±0.02	7.50 ^{+0.28} _{-0.24}	0.95 ^{+0.01} _{-0.01}	0.06±0.01	-0.08±0.01	-0.13±0.01
4308	3497	5688±6	4.40±0.02	-0.319±0.004	1.00±0.01	10.40 ^{+0.29} _{-0.24}	0.91 ^{+0.02} _{-0.02}	0.22±0.01	-0.12±0.01	-0.34±0.01
4597	3704	6027±12	4.36±0.03	-0.432±0.009	1.42±0.03	7.60 ^{+0.25} _{-0.21}	0.96 ^{+0.01} _{-0.01}	0.09±0.01	-0.13±0.01	-0.22±0.01
7134	5578	5992±9	4.52±0.02	-0.315±0.005	1.24±0.02	6.60 ^{+0.77} _{-0.30}	0.99 ^{+0.01} _{-0.01}	0.10±0.01	-0.03±0.01	-0.13±0.02
17548	13128	6004±14	4.36±0.04	-0.586±0.010	1.50±0.04	9.50 ^{+0.30} _{-0.28}	0.89 ^{+0.02} _{-0.02}	0.12±0.01	-0.16±0.01	-0.28±0.02
17865	13267	5882±11	4.25±0.03	-0.631±0.008	1.39±0.03	10.90 ^{+0.29} _{-0.28}	0.90 ^{+0.01} _{-0.01}	0.25±0.01	-0.11±0.01	-0.35±0.01
20407	15131	5877±8	4.47±0.02	-0.458±0.006	1.27±0.02	8.60 ^{+0.27} _{-0.27}	0.88 ^{+0.01} _{-0.01}	0.08±0.01	-0.11±0.01	-0.19±0.01
21938	16365	5812±8	4.40±0.02	-0.484±0.007	1.24±0.02	11.00 ^{+0.27} _{-0.24}	0.90 ^{+0.01} _{-0.01}	0.25±0.01	-0.11±0.01	-0.36±0.01
26887	19809	6045±11	4.42±0.03	-0.395±0.008	1.40±0.02	7.00 ^{+0.24} _{-0.23}	0.97 ^{+0.01} _{-0.01}	0.07±0.01	-0.10±0.01	-0.17±0.01
28701	20677	5742±6	4.41±0.02	-0.320±0.004	1.07±0.01	10.40 ^{+0.25} _{-0.25}	0.93 ^{+0.01} _{-0.01}	0.25±0.01	0.23±0.01	-0.02±0.01
40865	28403	5727±5	4.47±0.02	-0.390±0.004	1.05±0.01	10.20 ^{+0.35} _{-0.39}	0.87 ^{+0.02} _{-0.01}	0.10±0.00	-0.14±0.01	-0.24±0.01
41248	28460	5746±8	4.50±0.02	-0.361±0.006	1.02±0.01	7.30 ^{+0.57} _{-0.28}	0.88 ^{+0.02} _{-0.02}	0.06±0.00	-0.03±0.01	-0.08±0.01
41323	28604	5774±12	4.51±0.02	-0.309±0.009	1.01±0.02	5.20 ^{+0.64} _{-0.28}	0.92 ^{+0.01} _{-0.01}	0.04±0.01	-0.01±0.01	-0.05±0.01
48938	32322	6029±12	4.38±0.03	-0.425±0.009	1.44±0.03	7.90 ^{+0.28} _{-0.28}	0.96 ^{+0.01} _{-0.01}	0.09±0.01	-0.13±0.01	-0.22±0.01
56274	35139	5777±11	4.56±0.02	-0.539±0.009	1.14±0.02	8.40 ^{+0.28} _{-0.28}	0.84 ^{+0.02} _{-0.02}	0.07±0.01	-0.10±0.01	-0.17±0.01
61902	37240	6148±19	4.14±0.05	-0.710±0.013	1.82±0.07	8.10 ^{+0.38} _{-0.28}	0.95 ^{+0.02} _{-0.02}	0.11±0.02	-0.14±0.01	-0.25±0.02
61986	37419	5742±6	4.45±0.02	-0.359±0.004	1.07±0.01	10.30 ^{+0.24} _{-0.24}	0.88 ^{+0.02} _{-0.02}	0.09±0.01	-0.15±0.00	-0.25±0.00
65907	38908	5992±9	4.52±0.02	-0.315±0.005	1.24±0.02	4.60 ^{+0.53} _{-0.68}	1.02 ^{+0.01} _{-0.02}	0.23±0.01	-0.09±0.01	-0.32±0.01
78558	44860	5757±8	4.36±0.02	-0.435±0.007	1.14±0.01	11.70 ^{+0.28} _{-0.25}	0.90 ^{+0.02} _{-0.01}	0.28±0.01	-0.04±0.01	-0.32±0.01
87838	49615	6094±12	4.35±0.03	-0.456±0.008	1.53±0.03	6.90 ^{+0.41} _{-0.28}	0.98 ^{+0.02} _{-0.02}	0.10±0.01	-0.13±0.01	-0.23±0.02
94444	53244	6013±16	4.26±0.04	-0.647±0.011	1.52±0.04	10.10 ^{+0.31} _{-0.28}	0.89 ^{+0.01} _{-0.01}	0.09±0.01	-0.15±0.01	-0.24±0.01
97507	54779	5774±8	4.37±0.02	-0.392±0.006	1.15±0.01	11.30 ^{+0.26} _{-0.26}	0.91 ^{+0.02} _{-0.02}	0.24±0.01	-0.09±0.01	-0.32±0.01
97998	55013	5702±8	4.51±0.02	-0.446±0.006	1.01±0.02	8.90 ^{+0.27} _{-0.27}	0.84 ^{+0.01} _{-0.01}	0.07±0.01	-0.07±0.01	-0.14±0.01
102365	57443	5647±4	4.40±0.01	-0.318±0.003	0.98±0.01	10.50 ^{+0.22} _{-0.41}	0.88 ^{+0.01} _{-0.01}	0.15±0.01	-0.14±0.01	-0.29±0.01
105837	59380	5920±9	4.49±0.03	-0.532±0.006	1.33±0.02	9.40 ^{+0.27} _{-0.27}	0.87 ^{+0.01} _{-0.01}	0.09±0.01	-0.14±0.01	-0.23±0.01
109310	61323	5912±10	4.46±0.03	-0.530±0.007	1.30±0.02	10.10 ^{+0.28} _{-0.28}	0.87 ^{+0.01} _{-0.01}	0.09±0.01	-0.15±0.01	-0.24±0.01
109684	61539	6012±12	4.32±0.03	-0.370±0.009	1.46±0.02	7.50 ^{+0.49} _{-0.21}	0.99 ^{+0.01} _{-0.01}	0.08±0.01	-0.14±0.01	-0.22±0.02
117105	65737	5904±8	4.33±0.02	-0.300±0.006	1.25±0.02	8.80 ^{+0.21} _{-0.35}	0.96 ^{+0.02} _{-0.02}	0.10±0.01	-0.14±0.01	-0.24±0.01
119173	66815	5888±13	4.42±0.03	-0.670±0.009	1.34±0.03	12.00 ^{+0.36} _{-0.28}	0.82 ^{+0.02} _{-0.02}	0.12±0.01	-0.18±0.01	-0.31±0.01
123651	69202	5922±8	4.46±0.03	-0.509±0.006	1.30±0.02	8.80 ^{+0.69} _{-0.21}	0.88 ^{+0.02} _{-0.02}	0.10±0.01	-0.12±0.01	-0.22±0.01
136352	75181	5708±5	4.44±0.02	-0.340±0.004	1.04±0.01	10.90 ^{+0.27} _{-0.52}	0.90 ^{+0.02} _{-0.01}	0.22±0.01	-0.09±0.01	-0.31±0.01
141624	77818	5914±7	4.40±0.02	-0.401±0.006	1.28±0.02	8.70 ^{+0.21} _{-0.35}	0.93 ^{+0.01} _{-0.02}	0.11±0.01	-0.16±0.01	-0.27±0.01
143114	78330	5804±10	4.38±0.03	-0.426±0.008	1.16±0.02	10.60 ^{+0.86} _{-0.28}	0.91 ^{+0.02} _{-0.02}	0.22±0.01	-0.09±0.01	-0.32±0.01
148211	80587	5917±12	4.21±0.03	-0.660±0.008	1.51±0.03	10.80 ^{+0.28} _{-0.28}	0.89 ^{+0.02} _{-0.02}	0.21±0.01	-0.11±0.01	-0.32±0.01
150433	81681	5683±6	4.41±0.02	-0.371±0.004	1.03±0.01	11.30 ^{+0.23} _{-0.23}	0.89 ^{+0.01} _{-0.01}	0.26±0.01	-0.11±0.00	-0.36±0.01
162396	87523	6077±14	4.18±0.03	-0.399±0.010	1.60±0.03	6.60 ^{+0.57} _{-0.38}	1.05 ^{+0.01} _{-0.01}	0.09±0.01	-0.01±0.01	-0.10±0.02
172568	91805	5727±7	4.49±0.02	-0.394±0.005	1.05±0.01	9.10 ^{+0.29} _{-0.29}	0.87 ^{+0.01} _{-0.01}	0.09±0.00	-0.14±0.01	-0.23±0.01
177758	93827	5874±10	4.31±0.03	-0.630±0.007	1.41±0.02	12.10 ^{+0.27} _{-0.27}	0.87 ^{+0.01} _{-0.01}	0.25±0.01	-0.11±0.01	-0.36±0.01
181720	95262	5792±12	4.17±0.03	-0.558±0.009	1.39±0.02	10.40 ^{+0.29} _{-0.29}	0.94 ^{+0.01} _{-0.01}	0.25±0.01	-0.13±0.01	-0.38±0.01
188815	98355	6210±18	4.27±0.05	-0.599±0.012	1.81±0.06	7.10 ^{+0.26} _{-0.30}	0.97 ^{+0.01} _{-0.01}	0.07±0.01	-0.10±0.02	-0.16±0.02
197536	102339	6082±13	4.27±0.03	-0.466±0.009	1.61±0.03	7.50 ^{+0.25} _{-0.25}	0.99 ^{+0.01} _{-0.01}	0.09±0.01	-0.11±0.01	-0.2±0.02
203608	105858	6139±15	4.40±0.04	-0.685±0.010	1.64±0.05	7.80 ^{+0.36} _{-0.31}	0.91 ^{+0.01} _{-0.01}	0.09±0.01	-0.13±0.01	-0.22±0.02
207190	107599	6178±15	4.22±0.03	-0.470±0.010	1.72±0.04	6.40 ^{+0.28} _{-0.28}	1.04 ^{+0.01} _{-0.01}	0.07±0.01	-0.08±0.02	-0.15±0.02
210752	109646	5936±11	4.41±0.03	-0.627±0.008	1.39±0.03	11.20 ^{+0.27} _{-0.16}	0.85 ^{+0.01} _{-0.02}	0.09±0.01	-0.15±0.01	-0.24±0.01
214385	111746	5695±5	4.45±0.02	-0.347±0.003	1.01±0.05	9.70 ^{+0.62} _{-0.21}	0.87 ^{+0.01} _{-0.01}	0.09±0.01	-0.14±0.01	-0.23±0.01
215257	112229	6027±16	4.29±0.04	-0.690±0.011	1.63±0.05	10.20 ^{+0.32} _{-0.32}	0.88 ^{+0.01} _{-0.01}	0.11±0.02	-0.16±0.01	-0.27±0.02
218504	114276	5953±13	4.25±0.03	-0.602±0.009	1.49±0.03	10.30 ^{+0.29} _{-0.29}	0.91 ^{+0.01} _{-0.01}	0.16±0.01	-0.13±0.01	-0.29±0.01
224393	118123	5776±11	4.50±0.02	-0.395±0.008	1.06±0.02	6.00 ^{+0.60} _{-0.69}	0.89 ^{+0.01} _{-0.02}	0.06±0.01	-0.03±0.01	-0.08±0.01

Table A.2: Stellar atmospheric parameters, mass, age, and the elemental abundance ratios of the solar-twins and analogues.

HD	HIP	T_{eff} (K)	log g (dex)	[Fe/H] (dex)	ζ (km s ⁻¹)	Age (Gyr)	Mass (M_{\odot})	[Mg/Fe] (dex)	[Y/Fe] (dex)	[Y/Mg] (dex)
361	669	5902±7	4.52±0.01	-0.122±0.005	1.10±0.01	1.60 ^{+0.42} _{-0.30}	1.02 ^{+0.02} _{-0.01}	-0.02±0.02	0.06±0.01	0.08±0.03
1233	1292	5549±18	4.55±0.03	0.151±0.015	1.10±0.04	0.40 ^{+0.40} _{-0.20}	0.99 ^{+0.02} _{-0.02}	-0.07±0.01	0.10±0.04	0.16±0.04
1461	1499	5751±4	4.33±0.01	0.182±0.003	1.01±0.01	4.70 ^{+0.38} _{-0.35}	1.07 ^{+0.01} _{-0.01}	0.00±0.01	-0.03±0.01	-0.03±0.02
2071	1954	5720±2	4.46±0.01	-0.090±0.003	0.96±0.01	4.80 ^{+0.39} _{-0.34}	0.97 ^{+0.01} _{-0.01}	0.01±0.01	0.03±0.01	0.02±0.01
3821	3203	5868±9	4.54±0.02	-0.050±0.007	1.16±0.02	0.53 ^{+0.34} _{-0.24}	1.04 ^{+0.01} _{-0.01}	-0.04±0.01	0.10±0.01	0.14±0.02
3964	3311	5734±3	4.47±0.01	0.064±0.003	0.96±0.01	3.40 ^{+0.34} _{-0.44}	1.01 ^{+0.01} _{-0.01}	-0.01±0.01	0.04±0.01	0.05±0.01
6204	4909	5861±7	4.50±0.02	0.048±0.006	1.11±0.01	0.90 ^{+0.31} _{-0.23}	1.06 ^{+0.01} _{-0.01}	-0.05±0.01	0.09±0.01	0.14±0.01
6718	5301	5723±3	4.40±0.01	-0.074±0.003	0.98±0.01	6.90 ^{+0.23} _{-0.23}	0.96 ^{+0.01} _{-0.01}	0.02±0.00	-0.02±0.01	-0.04±0.01
7661	5938	5450±14	4.52±0.02	0.032±0.010	1.08±0.03	3.70 ^{+0.71} _{-0.34}	0.92 ^{+0.03} _{-0.03}	-0.05±0.02	0.11±0.03	0.16±0.04
BD-12 243	6276	5384±18	4.54±0.03	-0.014±0.012	1.14±0.03	3.60 ^{+1.38} _{-0.26}	0.89 ^{+0.02} _{-0.02}	-0.09±0.03	0.08±0.03	0.18±0.04
8291	6407	5775±7	4.51±0.01	-0.058±0.006	0.98±0.01	2.00 ^{+0.78} _{-0.57}	1.00 ^{+0.01} _{-0.01}	-0.01±0.01	0.06±0.01	0.08±0.01
8406	6455	5731±4	4.48±0.01	-0.105±0.003	0.96±0.01	4.20 ^{+0.49} _{-0.30}	0.96 ^{+0.01} _{-0.01}	-0.01±0.01	0.05±0.01	0.06±0.02
8828	6762	5398±6	4.39±0.02	-0.142±0.005	0.72±0.02	10.40 ^{+0.35} _{-0.30}	0.85 ^{+0.01} _{-0.01}	0.04±0.01	-0.07±0.02	-0.12±0.02
8859	6744	5518±4	4.39±0.01	-0.069±0.004	0.82±0.01	7.20 ^{+0.26} _{-0.26}	0.91 ^{+0.01} _{-0.01}	0.03±0.01	-0.04±0.01	-0.07±0.01
9986	7585	5822±3	4.45±0.01	0.083±0.003	1.01±0.01	3.70 ^{+0.28} _{-0.25}	1.04 ^{+0.01} _{-0.01}	-0.01±0.00	0.06±0.00	0.07±0.01
10008	7576	5316±9	4.49±0.02	-0.055±0.008	0.93±0.03	6.00 ^{+0.44} _{-0.32}	0.86 ^{+0.01} _{-0.01}	-0.05±0.02	0.13±0.03	0.18±0.04
11195	8507	5717±3	4.46±0.01	-0.099±0.003	0.96±0.01	5.50 ^{+0.32} _{-0.32}	0.96 ^{+0.01} _{-0.01}	0.02±0.01	0.04±0.00	0.03±0.01
12264	9349	5818±6	4.52±0.01	-0.006±0.005	1.09±0.01	1.80 ^{+0.94} _{-0.55}	1.04 ^{+0.01} _{-0.01}	-0.03±0.01	0.06±0.01	0.10±0.01
13060	9400	5231±11	4.36±0.03	0.0						

Table A.2: continued

HD	HIP	T_{eff} (K)	log g (dex)	[Fe/H] (dex)	ζ (km s ⁻¹)	Age (Gyr)	Mass (M_{\odot})	[Mg/Fe] (dex)	[Y/Fe] (dex)	[Y/Mg] (dex)
16297	12119	5396±6	4.43±0.02	0.008±0.006	0.81±0.02	6.80 ^{+0.92} _{-0.49}	0.89 ^{+0.02} _{-0.01}	-0.02±0.01	0.07±0.02	0.09±0.03
17925	13402	5149±18	4.44±0.06	0.088±0.015	0.97±0.06	6.10 ^{+1.89} _{-0.89}	0.84 ^{+0.01} _{-0.01}	-0.09±0.02	0.13±0.06	0.22±0.06
19467	14501	5738±4	4.31±0.01	-0.153±0.003	1.07±0.01	9.80 ^{+0.25} _{-0.25}	0.98 ^{+0.01} _{-0.01}	0.17±0.01	-0.08±0.01	-0.25±0.01
19518	14614	5803±4	4.45±0.01	-0.109±0.004	1.03±0.01	5.60 ^{+0.38} _{-0.47}	0.99 ^{+0.01} _{-0.01}	0.01±0.01	0.02±0.01	0.01±0.01
19668	14684	5501±18	4.57±0.03	0.010±0.013	1.15±0.04	1.00 ^{+0.15} _{-0.15}	0.93 ^{+0.01} _{-0.01}	-0.08±0.02	0.09±0.05	0.18±0.06
20003	14530	5483±5	4.40±0.02	0.075±0.006	0.76±0.02	7.60 ^{+0.26} _{-0.26}	0.93 ^{+0.01} _{-0.01}	0.00±0.01	0.04±0.02	0.03±0.02
20782	15527	5779±4	4.34±0.01	-0.064±0.003	1.07±0.01	8.10 ^{+0.25} _{-0.25}	0.99 ^{+0.01} _{-0.01}	0.03±0.01	-0.12±0.00	-0.15±0.01
21693	16085	5447±6	4.41±0.02	0.044±0.006	0.73±0.02	7.40 ^{+0.27} _{-0.27}	0.91 ^{+0.01} _{-0.01}	0.03±0.01	0.02±0.02	-0.01±0.02
21175	15799	5223±12	4.35±0.03	0.127±0.010	0.69±0.04	10.30 ^{+1.02} _{-1.02}	0.86 ^{+0.01} _{-0.01}	0.00±0.02	0.03±0.03	0.03±0.03
25874	18844	5734±3	4.37±0.01	0.014±0.003	1.01±0.01	7.50 ^{+0.23} _{-0.23}	1.00 ^{+0.01} _{-0.01}	0.07±0.01	-0.08±0.01	-0.15±0.01
26913	19855	5692±14	4.56±0.03	0.015±0.010	1.20±0.03	0.40 ^{+0.88} _{-0.21}	0.99 ^{+0.01} _{-0.01}	-0.07±0.02	0.10±0.04	0.18±0.04
28185	20723	5655±6	4.32±0.02	0.232±0.007	0.96±0.02	4.40 ^{+0.39} _{-0.38}	1.04 ^{+0.01} _{-0.01}	0.02±0.01	-0.05±0.01	-0.07±0.01
30306	21731	5547±9	4.27±0.02	0.223±0.008	0.89±0.02	7.50 ^{+0.39} _{-0.39}	1.00 ^{+0.02} _{-0.02}	0.03±0.01	-0.06±0.03	-0.08±0.03
30495	22263	5870±7	4.54±0.01	0.037±0.006	1.10±0.01	0.63 ^{+0.34} _{-0.34}	1.05 ^{+0.01} _{-0.01}	-0.04±0.01	0.11±0.01	0.15±0.01
31527	22905	5907±5	4.38±0.02	-0.185±0.004	1.15±0.01	5.90 ^{+0.28} _{-0.28}	1.00 ^{+0.01} _{-0.01}	0.05±0.00	-0.07±0.01	-0.12±0.01
32724	23627	5826±8	4.16±0.02	-0.184±0.005	1.22±0.01	8.50 ^{+0.24} _{-0.24}	1.02 ^{+0.01} _{-0.01}	0.12±0.01	-0.12±0.01	-0.24±0.01
34449	22504	5854±3	4.47±0.01	-0.098±0.003	1.07±0.01	2.70 ^{+0.29} _{-0.27}	1.01 ^{+0.01} _{-0.01}	-0.01±0.01	0.02±0.01	0.03±0.02
36152	25670	5760±3	4.42±0.01	0.054±0.003	0.98±0.01	5.10 ^{+0.27} _{-0.27}	1.01 ^{+0.01} _{-0.01}	0.01±0.01	0.02±0.01	0.01±0.01
39881	28066	5742±4	4.30±0.01	-0.147±0.003	1.07±0.01	9.00 ^{+0.26} _{-0.26}	0.99 ^{+0.01} _{-0.01}	0.19±0.01	-0.08±0.01	-0.27±0.01
40397	28267	5522±5	4.38±0.01	-0.116±0.004	0.84±0.01	11.30 ^{+0.24} _{-0.24}	0.89 ^{+0.01} _{-0.01}	0.13±0.01	-0.08±0.01	-0.21±0.01
41087	28518	5588±13	4.53±0.02	-0.105±0.009	1.07±0.02	2.90 ^{+0.09} _{-0.09}	0.93 ^{+0.01} _{-0.01}	-0.07±0.01	0.08±0.02	0.15±0.02
41593	28954	5306±14	4.49±0.03	0.034±0.011	0.93±0.04	4.50 ^{+0.92} _{-0.92}	0.88 ^{+0.02} _{-0.02}	-0.05±0.02	0.20±0.05	0.25±0.06
42618	29432	5762±3	4.45±0.01	-0.112±0.003	1.01±0.01	6.00 ^{+0.28} _{-0.28}	0.97 ^{+0.01} _{-0.01}	0.00±0.00	-0.02±0.00	-0.02±0.01
42807	29525	5741±9	4.52±0.02	-0.012±0.007	1.09±0.02	0.80 ^{+0.30} _{-0.30}	0.90 ^{+0.02} _{-0.02}	-0.06±0.01	0.09±0.01	0.14±0.01
43162	29568	5658±13	4.55±0.03	0.025±0.009	1.15±0.02	0.90 ^{+0.27} _{-0.27}	0.98 ^{+0.01} _{-0.01}	-0.08±0.02	0.10±0.03	0.18±0.04
43834	29271	5593±5	4.38±0.02	0.123±0.005	0.86±0.01	5.50 ^{+0.38} _{-0.38}	0.99 ^{+0.02} _{-0.02}	0.02±0.01	0.01±0.01	-0.01±0.02
45021	30037	5666±3	4.42±0.01	0.007±0.003	0.91±0.01	6.40 ^{+0.26} _{-0.26}	0.96 ^{+0.01} _{-0.01}	0.00±0.01	-0.02±0.01	-0.02±0.01
44665A	30158	5678±4	4.37±0.01	-0.004±0.003	0.95±0.01	7.30 ^{+0.29} _{-0.29}	0.96 ^{+0.01} _{-0.01}	0.03±0.01	-0.04±0.01	-0.08±0.01
45289	30476	5709±4	4.28±0.01	-0.033±0.003	1.05±0.01	9.40 ^{+0.26} _{-0.26}	0.99 ^{+0.01} _{-0.01}	0.11±0.01	-0.10±0.01	-0.21±0.01
45346	30502	5731±4	4.40±0.01	-0.057±0.004	0.98±0.01	7.30 ^{+0.29} _{-0.29}	0.97 ^{+0.01} _{-0.01}	0.02±0.01	-0.03±0.01	-0.02±0.01
47186	31540	5674±6	4.33±0.02	0.253±0.007	0.97±0.02	4.30 ^{+0.37} _{-0.37}	1.06 ^{+0.01} _{-0.01}	0.00±0.01	-0.03±0.01	-0.04±0.02
50806	33094	5629±7	4.11±0.02	0.023±0.005	1.10±0.01	8.70 ^{+0.09} _{-0.09}	1.06 ^{+0.01} _{-0.01}	-0.07±0.01	0.16±0.01	0.16±0.01
51608	33229	5370±6	4.38±0.02	-0.023±0.006	0.70±0.02	10.40 ^{+0.95} _{-0.25}	0.86 ^{+0.01} _{-0.01}	0.05±0.01	-0.05±0.03	-0.10±0.04
53705	34065	5826±8	4.29±0.02	-0.230±0.006	1.17±0.02	9.20 ^{+0.02} _{-0.02}	0.99 ^{+0.01} _{-0.01}	0.13±0.01	-0.14±0.01	-0.27±0.02
54351	34511	5812±4	4.45±0.01	-0.091±0.003	1.04±0.01	5.20 ^{+0.46} _{-0.46}	1.00 ^{+0.01} _{-0.01}	0.01±0.01	0.03±0.01	0.02±0.01
59468	36210	5617±4	4.39±0.01	0.045±0.004	0.91±0.01	7.60 ^{+0.35} _{-0.35}	0.96 ^{+0.03} _{-0.03}	0.03±0.01	-0.06±0.01	-0.09±0.01
59711	36512	5744±2	4.45±0.01	-0.126±0.002	0.99±0.01	6.30 ^{+0.25} _{-0.25}	0.96 ^{+0.01} _{-0.01}	0.02±0.01	-0.01±0.00	-0.03±0.01
59967	36515	5855±12	4.56±0.02	-0.029±0.009	1.23±0.02	0.50 ^{+0.24} _{-0.24}	1.03 ^{+0.01} _{-0.01}	-0.07±0.01	0.09±0.01	0.16±0.02
61005	36948	5581±20	4.51±0.04	0.069±0.015	1.43±0.04	3.60 ^{+0.18} _{-0.18}	0.96 ^{+0.01} _{-0.01}	-0.07±0.02	0.03±0.06	0.10±0.06
63487	38072	5860±9	4.51±0.02	0.085±0.007	1.15±0.02	2.10 ^{+0.36} _{-0.36}	1.06 ^{+0.01} _{-0.01}	-0.02±0.01	0.03±0.01	0.06±0.01
63765	38041	5445±4	4.48±0.02	-0.137±0.004	0.81±0.01	5.60 ^{+0.35} _{-0.35}	0.88 ^{+0.02} _{-0.02}	-0.01±0.02	0.06±0.01	0.07±0.03
65216	38558	5634±4	4.47±0.01	-0.155±0.004	0.91±0.01	5.20 ^{+0.46} _{-0.46}	0.92 ^{+0.01} _{-0.01}	0.00±0.01	0.04±0.01	0.03±0.02
66221	39298	5625±6	4.32±0.02	0.202±0.007	0.93±0.02	6.00 ^{+0.69} _{-0.69}	1.03 ^{+0.01} _{-0.01}	0.04±0.01	-0.02±0.02	-0.06±0.02
66653	39330	5869±4	4.43±0.01	0.145±0.004	1.07±0.01	1.40 ^{+0.22} _{-0.22}	1.10 ^{+0.02} _{-0.02}	-0.03±0.00	0.01±0.01	0.04±0.01
67458	39710	5904±7	4.43±0.02	-0.172±0.006	1.13±0.02	3.30 ^{+0.39} _{-0.39}	1.02 ^{+0.01} _{-0.01}	0.03±0.01	-0.02±0.01	-0.05±0.01
68168	40133	5745±3	4.37±0.01	0.116±0.002	0.99±0.01	5.30 ^{+0.37} _{-0.37}	1.04 ^{+0.02} _{-0.02}	0.03±0.00	-0.01±0.00	-0.05±0.01
69830	40693	5399±5	4.41±0.02	-0.029±0.006	0.71±0.02	8.30 ^{+0.24} _{-0.24}	0.88 ^{+0.01} _{-0.01}	0.03±0.01	0.02±0.03	-0.01±0.03
70642	40952	5692±4	4.37±0.01	0.194±0.004	0.94±0.01	3.30 ^{+0.27} _{-0.27}	1.05 ^{+0.01} _{-0.01}	0.01±0.01	-0.01±0.01	-0.03±0.02
71334	41317	5706±3	4.39±0.01	-0.081±0.003	0.99±0.01	7.70 ^{+0.32} _{-0.32}	0.96 ^{+0.01} _{-0.01}	0.06±0.00	-0.08±0.01	-0.14±0.01
71835	41529	5464±4	4.44±0.01	0.005±0.004	0.78±0.01	7.30 ^{+0.25} _{-0.25}	0.90 ^{+0.01} _{-0.01}	0.00±0.01	0.03±0.02	0.03±0.02
72769	42011	5635±8	4.27±0.02	0.339±0.008	0.98±0.02	5.40 ^{+0.35} _{-0.35}	1.07 ^{+0.01} _{-0.01}	0.01±0.02	-0.02±0.01	-0.03±0.02
73350	42333	5846±8	4.50±0.02	0.132±0.006	1.11±0.01	0.90 ^{+0.29} _{-0.29}	1.07 ^{+0.01} _{-0.01}	-0.05±0.01	0.09±0.01	0.14±0.01
74014	42634	5570±9	4.29±0.02	0.262±0.008	0.91±0.02	6.30 ^{+0.40} _{-0.40}	1.02 ^{+0.02} _{-0.02}	0.02±0.02	-0.04±0.02	-0.06±0.03
75302	43297	5705±4	4.51±0.01	0.082±0.003	1.00±0.01	2.60 ^{+0.26} _{-0.26}	1.01 ^{+0.01} _{-0.01}	-0.02±0.01	0.09±0.01	0.11±0.01
76151	43726	5785±3	4.44±0.01	0.109±0.004	1.01±0.01	1.40 ^{+0.11} _{-0.11}	1.06 ^{+0.01} _{-0.01}	-0.02±0.00	-0.01±0.01	0.01±0.01
78429	44713	5759±3	4.28±0.01	0.063±0.004	1.09±0.01	7.60 ^{+0.27} _{-0.27}	1.03 ^{+0.01} _{-0.01}	0.03±0.01	-0.10±0.01	-0.13±0.01
78534	44935	5771±4	4.37±0.01	0.038±0.004	1.04±0.01	6.60 ^{+0.26} _{-0.26}	1.01 ^{+0.01} _{-0.01}	0.03±0.00	-0.05±0.01	-0.08±0.01
78538	44890	5804±9	4.53±0.02	-0.006±0.006	1.07±0.01	0.40 ^{+0.94} _{-0.94}	1.02 ^{+0.02} _{-0.02}	-0.06±0.01	0.10±0.02	0.16±0.02
78612	44896	5846±9	4.18±0.02	-0.260±0.007	1.25±0.02	9.00 ^{+0.20} _{-0.20}	1.00 ^{+0.01} _{-0.01}	0.11±0.01	-0.12±0.01	-0.23±0.02
78660	44997	5728±3	4.41±0.01	-0.012±0.003	0.96±0.01	5.10 ^{+0.27} _{-0.27}	0.97 ^{+0.01} _{-0.01}	-0.01±0.00	0.01±0.01	0.02±0.01
83529	47225	5916±7	4.28±0.02	-0.244±0.005	1.23±0.01	6.90 ^{+0.42} _{-0.42}	1.00 ^{+0.01} _{-0.01}	0.07±0.01	-0.13±0.01	-0.20±0.02
88072	49756	5789±3	4.44±0.01	0.023±0.003	1.03±0.01	5.20 ^{+0.25} _{-0.25}	1.01 ^{+0.01} _{-0.01}	0.01±0.01	0.01±0.00	0.00±0.01
89454	50534	5732±4	4.50±0.01	0.139±0.004	0.98±0.01	1.40 ^{+0.66} _{-0.66}	1.03 ^{+0.01} _{-0.01}	-0.06±0.02	0.08±0.01	0.14±0.03
92719	52369	5812±3	4.47±0.01	-0.114±0.003	1.03±0.01	4.40 ^{+0.32} _{-0.32}	0.98 ^{+0.01} _{-0.01}	0.00±0.01	0.03±0.01	0.03±0.02
94151	53087	5618±3	4.43±0.01	0.072±0.003	0.89±0.01	5.50 ^{+0.40} _{-0.40}	0.97 ^{+0.01} _{-0.01}	0.01±0.01	0.03±0.01	0.01±0.01
95521	53837	5774±4	4.48±0.01	-0.155±0.004	1.02±0.01	5.00 ^{+0.39} _{-0.39}	0.96 ^{+0.02} _{-0.02}	0.00±0.01	0.03±0.01	0.03±0.02
96064	54155	5507±17	4.56±0.03	0.067±0.011	1.16±0.03	0.70 ^{+0.35} _{-0.35}	0.94 ^{+0.01} _{-0.01}	-0.07±0.02	0.12±0.04	0.19±0.04
96116	54102	5845±6	4.51±0.01	0.011±0.005	1.06±0.01	1.40 ^{+0.26} _{-0.26}	1.05 ^{+0.01} _{-0.01}	-0.04±0.01	0.08±0.01	0.12±0.01
96423	54287	5714±4	4.34±0.01	0.107±0.004	0.99±0.01	5.90 ^{+0.29} _{-0.29}	1.02 ^{+0.}			

Table A.2: continued

HD	HIP	T_{eff} (K)	log g (dex)	[Fe/H] (dex)	ζ (km s $^{-1}$)	Age (Gyr)	Mass (M_{\odot})	[Mg/Fe] (dex)	[Y/Fe] (dex)	[Y/Mg] (dex)
115169	64713	5788±4	4.44±0.01	-0.043±0.003	1.00±0.01	5.40 $^{+0.30}_{-0.44}$	0.99 $^{+0.02}_{-0.01}$	0.01±0.00	0.01±0.01	0.00±0.01
115617	64924	5568±4	4.39±0.01	0.006±0.004	0.84±0.01	7.70 $^{+0.43}_{-0.26}$	0.93 $^{+0.01}_{-0.01}$	0.03±0.01	-0.06±0.02	-0.08±0.02
117126	65708	5746±5	4.22±0.01	-0.063±0.005	1.12±0.01	9.10 $^{+0.25}_{-0.24}$	1.01 $^{+0.02}_{-0.01}$	0.11±0.01	-0.08±0.01	-0.19±0.01
117207	65808	5659±7	4.30±0.02	0.242±0.007	0.97±0.02	5.40 $^{+0.25}_{-0.29}$	1.05 $^{+0.02}_{-0.01}$	-0.01±0.02	-0.04±0.03	-0.03±0.03
122194	68468	5845±5	4.33±0.01	0.071±0.004	1.10±0.01	5.80 $^{+0.29}_{-0.27}$	1.06 $^{+0.01}_{-0.01}$	0.05±0.01	-0.05±0.01	-0.10±0.01
124292	69414	5458±4	4.39±0.01	-0.113±0.004	0.79±0.01	9.90 $^{+0.23}_{-0.46}$	0.87 $^{+0.01}_{-0.01}$	0.06±0.01	-0.08±0.02	-0.13±0.02
124523	69645	5751±3	4.44±0.01	-0.026±0.004	1.00±0.01	5.70 $^{+0.41}_{-0.41}$	0.99 $^{+0.01}_{-0.01}$	0.02±0.01	0.00±0.01	-0.02±0.01
126525	70695	5668±3	4.42±0.01	-0.075±0.003	0.94±0.01	6.50 $^{+0.46}_{-0.30}$	0.96 $^{+0.01}_{-0.01}$	0.05±0.01	-0.06±0.01	-0.11±0.01
129814	72043	5845±4	4.34±0.01	-0.026±0.003	1.12±0.01	6.80 $^{+0.26}_{-0.27}$	1.03 $^{+0.02}_{-0.01}$	0.06±0.01	-0.10±0.01	-0.16±0.01
130322	72339	5368±7	4.42±0.02	0.036±0.007	0.74±0.02	7.30 $^{+0.70}_{-0.88}$	0.89 $^{+0.02}_{-0.01}$	0.00±0.01	0.07±0.03	0.07±0.03
131923	73241	5661±5	4.22±0.01	0.092±0.005	1.00±0.01	8.70 $^{+0.58}_{-0.50}$	1.03 $^{+0.01}_{-0.02}$	0.12±0.01	-0.09±0.01	-0.2±0.01
133600	73815	5790±3	4.33±0.01	0.023±0.003	1.07±0.01	7.30 $^{+0.29}_{-0.31}$	1.01 $^{+0.01}_{-0.01}$	0.03±0.01	-0.10±0.01	-0.13±0.01
134330	74271	5623±5	4.46±0.02	0.102±0.005	0.98±0.01	4.00 $^{+0.30}_{-0.29}$	0.98 $^{+0.01}_{-0.01}$	-0.02±0.01	0.05±0.02	0.07±0.03
134606	74653	5625±9	4.29±0.02	0.311±0.008	0.97±0.02	5.50 $^{+0.29}_{-0.31}$	1.06 $^{+0.01}_{-0.01}$	0.02±0.02	-0.03±0.02	-0.06±0.03
134664	74389	5845±3	4.44±0.01	0.083±0.003	1.05±0.01	3.50 $^{+0.43}_{-0.42}$	1.05 $^{+0.01}_{-0.01}$	-0.01±0.01	0.04±0.01	0.04±0.01
135101	74432	5679±5	4.17±0.01	0.048±0.005	1.09±0.01	8.50 $^{+0.42}_{-0.25}$	1.06 $^{+0.01}_{-0.01}$	0.14±0.01	-0.09±0.01	-0.23±0.01
136894	75363	5451±5	4.39±0.02	-0.062±0.006	0.79±0.02	8.30 $^{+0.43}_{-0.43}$	0.89 $^{+0.01}_{-0.01}$	0.02±0.01	-0.06±0.03	-0.08±0.03
138549	76200	5586±3	4.45±0.01	0.032±0.005	0.89±0.01	4.70 $^{+0.25}_{-0.25}$	0.96 $^{+0.01}_{-0.01}$	0.00±0.01	0.02±0.01	0.02±0.01
138573	76114	5740±3	4.41±0.01	-0.024±0.003	0.97±0.01	6.50 $^{+0.29}_{-0.35}$	0.98 $^{+0.01}_{-0.01}$	0.01±0.00	-0.03±0.01	-0.04±0.01
140538	77052	5687±3	4.45±0.01	0.051±0.003	0.96±0.01	3.90 $^{+0.35}_{-0.34}$	0.99 $^{+0.01}_{-0.01}$	0.00±0.01	0.08±0.01	0.08±0.01
140901	77358	5619±4	4.43±0.02	0.107±0.004	0.95±0.01	4.40 $^{+0.31}_{-0.36}$	0.98 $^{+0.01}_{-0.01}$	-0.01±0.01	0.03±0.02	0.04±0.02
142331	77883	5699±3	4.38±0.01	0.017±0.003	0.99±0.01	7.60 $^{+0.23}_{-0.29}$	0.97 $^{+0.01}_{-0.01}$	0.02±0.01	-0.08±0.01	-0.10±0.01
145809	79524	5758±9	4.04±0.02	-0.296±0.008	1.25±0.01	8.50 $^{+0.28}_{-0.34}$	1.03 $^{+0.01}_{-0.01}$	0.12±0.01	-0.14±0.01	-0.26±0.02
145825	79578	5810±3	4.47±0.01	0.048±0.003	1.02±0.01	3.20 $^{+0.31}_{-0.33}$	1.03 $^{+0.01}_{-0.01}$	-0.01±0.01	0.03±0.01	0.04±0.01
145927	79715	5816±4	4.38±0.01	-0.037±0.004	1.09±0.01	6.70 $^{+0.33}_{-0.32}$	1.02 $^{+0.01}_{-0.01}$	0.08±0.01	-0.07±0.01	-0.15±0.01
146233	79672	5808±3	4.44±0.01	0.041±0.003	1.02±0.01	4.30 $^{+0.27}_{-0.28}$	1.00 $^{+0.01}_{-0.01}$	-0.05±0.00	0.04±0.01	0.09±0.01
147512	80218	5535±4	4.41±0.01	-0.061±0.004	0.81±0.01	8.30 $^{+0.38}_{-0.39}$	0.91 $^{+0.02}_{-0.01}$	0.05±0.01	-0.05±0.01	-0.09±0.02
149661	81300	5248±10	4.45±0.03	0.012±0.011	0.89±0.04	1.80 $^{+0.19}_{-0.19}$	0.91 $^{+0.01}_{-0.01}$	-0.03±0.02	0.06±0.02	0.09±0.03
150248	81746	5715±3	4.37±0.01	-0.091±0.003	0.99±0.01	8.10 $^{+0.24}_{-0.39}$	0.96 $^{+0.01}_{-0.01}$	0.06±0.00	-0.10±0.01	-0.16±0.01
151504	82265	5443±6	4.34±0.02	0.098±0.006	0.72±0.02	9.10 $^{+0.23}_{-0.23}$	0.93 $^{+0.01}_{-0.01}$	0.06±0.02	-0.01±0.02	-0.07±0.03
152391	82588	5483±10	4.53±0.02	-0.003±0.008	0.97±0.02	0.90 $^{+0.05}_{-0.33}$	0.94 $^{+0.01}_{-0.01}$	-0.04±0.02	0.11±0.03	0.15±0.04
153631	83276	5886±6	4.24±0.02	-0.093±0.005	1.23±0.01	6.60 $^{+0.33}_{-0.32}$	1.03 $^{+0.01}_{-0.01}$	0.02±0.01	-0.14±0.01	-0.16±0.01
157172	85017	5435±7	4.34±0.02	0.140±0.006	0.73±0.02	7.40 $^{+0.32}_{-0.32}$	0.94 $^{+0.01}_{-0.01}$	0.03±0.01	0.01±0.02	-0.02±0.03
157347	85042	5685±3	4.35±0.01	0.030±0.003	0.97±0.01	7.20 $^{+0.36}_{-0.26}$	0.97 $^{+0.01}_{-0.01}$	0.03±0.00	-0.04±0.01	-0.07±0.01
161612	87116	5620±5	4.42±0.02	0.200±0.007	0.85±0.02	2.60 $^{+0.80}_{-0.81}$	1.03 $^{+0.01}_{-0.01}$	0.03±0.01	-0.03±0.01	-0.05±0.01
162236	87369	5365±6	4.43±0.02	-0.076±0.005	0.79±0.02	6.00 $^{+1.01}_{-0.30}$	0.87 $^{+0.02}_{-0.01}$	-0.01±0.01	0.03±0.02	0.04±0.03
163441	87769	5828±3	4.40±0.01	0.072±0.004	1.03±0.01	5.00 $^{+0.30}_{-0.39}$	1.04 $^{+0.01}_{-0.01}$	0.01±0.01	0.01±0.01	0.00±0.01
167060	89650	5851±3	4.42±0.01	-0.015±0.003	1.10±0.01	5.60 $^{+0.39}_{-0.24}$	1.03 $^{+0.01}_{-0.01}$	0.04±0.01	-0.05±0.01	-0.08±0.01
168746	90004	5592±5	4.36±0.01	-0.09±0.005	0.90±0.01	10.30 $^{+0.24}_{-0.26}$	0.94 $^{+0.01}_{-0.01}$	0.18±0.01	-0.04±0.01	-0.22±0.02
171665	91287	5667±3	4.44±0.01	-0.037±0.003	0.94±0.01	4.80 $^{+0.35}_{-0.36}$	0.96 $^{+0.01}_{-0.01}$	0.00±0.01	0.02±0.01	0.02±0.02
172513	91700	5525±4	4.46±0.01	-0.023±0.004	0.86±0.01	5.70 $^{+0.46}_{-0.46}$	0.92 $^{+0.01}_{-0.01}$	-0.01±0.01	0.08±0.02	0.09±0.03
183658	95962	5805±3	4.38±0.01	0.029±0.003	1.04±0.01	5.90 $^{+0.28}_{-0.27}$	1.01 $^{+0.02}_{-0.01}$	0.02±0.00	-0.03±0.00	-0.04±0.01
183579	96160	5798±4	4.48±0.01	-0.036±0.003	1.02±0.01	3.10 $^{+0.37}_{-0.37}$	1.01 $^{+0.01}_{-0.01}$	0.00±0.01	0.05±0.01	0.05±0.01
185615	96854	5578±7	4.28±0.02	0.11±0.007	0.93±0.02	8.90 $^{+0.37}_{-0.45}$	0.97 $^{+0.01}_{-0.01}$	0.11±0.02	-0.07±0.01	-0.17±0.02
186302	97507	5694±6	4.48±0.02	0.007±0.007	0.92±0.02	4.70 $^{+0.46}_{-0.47}$	0.98 $^{+0.01}_{-0.01}$	0.00±0.01	0.04±0.01	0.04±0.02
186803	97358	5684±9	4.54±0.02	-0.009±0.007	0.96±0.02	1.10 $^{+0.64}_{-0.30}$	0.99 $^{+0.01}_{-0.01}$	-0.05±0.01	0.11±0.03	0.16±0.03
188748	98621	5629±4	4.42±0.01	-0.114±0.004	0.92±0.01	7.80 $^{+0.30}_{-0.27}$	0.92 $^{+0.01}_{-0.01}$	0.04±0.01	-0.05±0.02	-0.09±0.02
190647	99115	5615±11	4.09±0.02	0.242±0.009	1.07±0.02	8.50 $^{+0.25}_{-0.26}$	1.08 $^{+0.01}_{-0.01}$	0.06±0.02	-0.05±0.02	-0.11±0.03
196390	101905	5906±5	4.50±0.01	0.088±0.004	1.08±0.01	1.40 $^{+0.28}_{-0.28}$	1.08 $^{+0.02}_{-0.01}$	-0.03±0.01	0.08±0.01	0.11±0.01
197027	102152	5718±4	4.33±0.01	-0.016±0.003	0.99±0.01	8.40 $^{+0.23}_{-0.32}$	0.98 $^{+0.01}_{-0.01}$	0.03±0.01	-0.10±0.01	-0.14±0.01
197076	102040	5853±4	4.48±0.01	-0.080±0.003	1.05±0.01	2.60 $^{+0.43}_{-0.37}$	1.02 $^{+0.01}_{-0.01}$	0.00±0.00	0.05±0.01	0.05±0.01
197210	102203	5583±3	4.47±0.01	-0.009±0.004	0.85±0.01	4.70 $^{+0.35}_{-0.35}$	0.94 $^{+0.01}_{-0.01}$	-0.01±0.01	0.06±0.01	0.07±0.02
197823	102580	5400±7	4.40±0.02	0.164±0.007	0.79±0.02	4.40 $^{+0.47}_{-0.47}$	0.94 $^{+0.01}_{-0.01}$	0.00±0.01	0.07±0.03	0.07±0.03
198075	102664	5829±6	4.45±0.02	-0.283±0.005	1.10±0.01	4.20 $^{+0.36}_{-0.36}$	0.96 $^{+0.01}_{-0.01}$	0.04±0.01	-0.05±0.01	-0.10±0.02
200633	104045	5826±3	4.41±0.01	0.051±0.003	1.04±0.01	5.00 $^{+0.34}_{-0.38}$	1.03 $^{+0.02}_{-0.01}$	-0.01±0.00	0.02±0.01	0.03±0.01
201219	104318	5669±11	4.54±0.02	0.132±0.008	1.02±0.02	0.50 $^{+0.38}_{-0.36}$	1.03 $^{+0.01}_{-0.01}$	-0.03±0.01	0.04±0.02	0.07±0.02
202628	105184	5843±6	4.51±0.01	0.003±0.004	1.05±0.01	1.20 $^{+0.45}_{-0.45}$	1.05 $^{+0.01}_{-0.01}$	-0.01±0.01	0.10±0.01	0.11±0.01
203384	105483	5560±10	4.31±0.02	0.276±0.010	0.94±0.03	5.40 $^{+0.32}_{-0.32}$	1.02 $^{+0.02}_{-0.01}$	0.02±0.01	-0.04±0.02	-0.07±0.02
203432	105606	5646±6	4.37±0.02	0.328±0.007	1.01±0.02	3.40 $^{+0.37}_{-0.37}$	1.06 $^{+0.02}_{-0.01}$	-0.01±0.02	-0.05±0.02	-0.03±0.03
204313	106006	5760±5	4.32±0.01	0.181±0.005	1.03±0.01	4.50 $^{+0.24}_{-0.30}$	1.07 $^{+0.01}_{-0.01}$	0.00±0.01	-0.05±0.01	-0.05±0.02
205536	107022	5438±5	4.39±0.02	-0.021±0.006	0.73±0.02	9.00 $^{+0.30}_{-0.29}$	0.89 $^{+0.01}_{-0.01}$	0.05±0.01	-0.04±0.01	-0.10±0.01
205891	106931	5574±4	4.40±0.01	-0.138±0.004	0.86±0.01	8.60 $^{+0.32}_{-0.24}$	0.90 $^{+0.02}_{-0.01}$	0.05±0.01	-0.06±0.02	-0.11±0.03
207700	108158	5675±4	4.29±0.01	0.055±0.003	1.01±0.01	8.10 $^{+0.33}_{-0.24}$	1.02 $^{+0.01}_{-0.01}$	0.14±0.01	-0.08±0.01	-0.22±0.01
207832	107985	5730±4	4.44±0.01	0.154±0.004	1.01±0.01	1.20 $^{+0.25}_{-0.41}$	1.07 $^{+0.01}_{-0.01}$	-0.02±0.00	0.01±0.01	0.03±0.01
207970	108065	5562±6	4.32±0.02	0.086±0.005	0.89±0.01	10.90 $^{+0.41}_{-0.29}$	0.92 $^{+0.02}_{-0.01}$	0.08±0.01	-0.06±0.02	-0.14±0.02
208704	108468	5841±4	4.35±0.01	-0.096±0.004	1.13±0.01	7.20 $^{+0.26}_{-0.25}$	1.01 $^{+0.01}_{-0.01}$	0.04±0.01	-0.12±0.01	-0.16±0.01
210277	109378	5513±10	4.26±0.03	0.205±0.011	0.91±0.03	8.60 $^{+0.88}_{-0.85}$	0.98 $^{+0.02}_{-0.01}$	0.08±0.02	-0.02±0.02	-0.10±0.03
210918	109821	5747±4	4.31±0.01	-0.108±0.004	1.06±0.01	8.90 $^{+0.23}_{-0.23}$	0.98 $^{+0.01}_{-0.01}$	0.08±0.01	-0.09±0.01	-0.17±0.01
211415	110109	5871±5	4.38±0.02	-0.230±0.004	1.15±0.01	6.50 $^{+0.30}_{-0.31}$	0.98 $^{+0.01}_{-0.01}$	0.06±0.01	-0.11±0.01	-

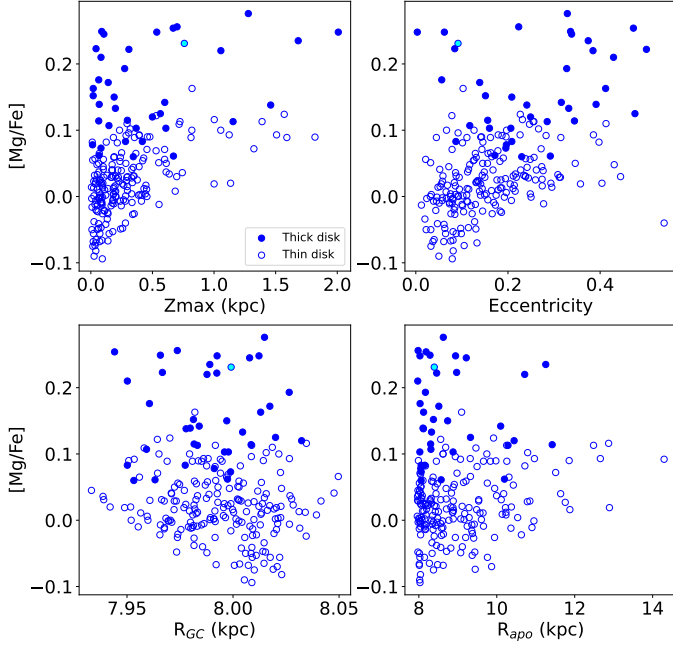


Fig. B.1: Observed $[Mg/Fe]$ of the entire sample with respect to various orbital parameters. The cyan circle is the anomalous star HD 65907.

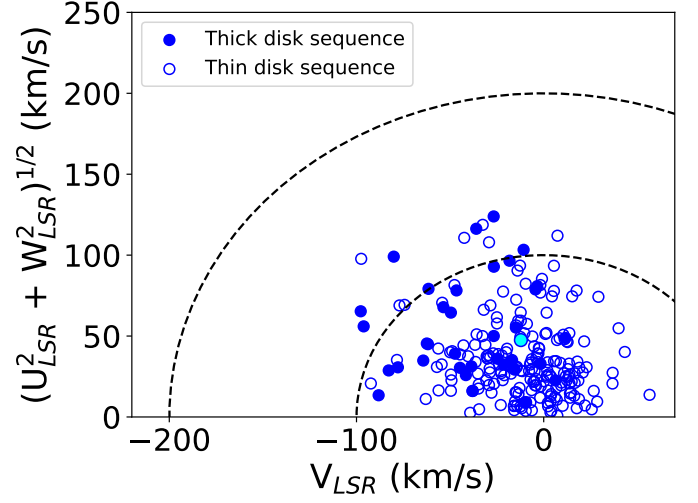


Fig. B.2: Toomre diagram for the entire sample. The dotted inner and outer circles have radii of 100 km/s and 200 km/s, respectively.

Appendix B: Kinematics of the stellar sample

Various orbital characteristics and Galactic space velocities of the sample are calculated using the `galpy`⁸ Python package (Bovy 2015). The components of spatial velocities (U , V , and W) are calculated with respect to the local standard of rest (LSR). The adopted solar motion about the LSR is $(U, V, W)_{\odot} = (11.1, 12.2, 7.3)$ km/s (Schönrich et al. 2010). The detailed procedure can be found in Shejeelammal & Goswami (2024). The behaviour of the $[Mg/Fe]$ ratio observed in the sample as functions of maximum height above the Galactic plane (Z_{max}), eccentricity, Galactocentric distance (R_{GC}) and apocentric distance (R_{apo}) are shown in Fig. B.1. The Toomre diagram for the sample is shown in Fig. B.2. As can be seen, it is difficult to separate the thin and thick disk from purely kinematic criteria.

⁸ <http://github.com/jobovy/galpy>